Tissue-resident macrophages favor early lung cancer development via direct physical interactions with cancer cells

Philippe Benaroch

benaroch@curie.fr

Institut Curie https://orcid.org/0000-0002-2655-0129

Jovan Nikolic

Institut Curie https://orcid.org/0000-0003-4119-7009

Ackermann Joseph

ENS, Université PSL*, CNRS, Sorbonne Université

Sarah Taheraly

Institut Curie

Morgane Mabire

Institut Curie

François-Xavier Gobert

Institut Curie

Apolline De Folmont

Institut Curie https://orcid.org/0009-0009-6460-9046

Ronan Thibaut

Institut Curie

Mathieu Morin

Institut Curie

Ouardia Ait-Mohamed

Institut de biologie de l'Ecole normale supérieure (IBENS) https://orcid.org/0000-0002-7637-6958

Edison Gerena

Sorbonne Université, CNRS.

Sophie Goyard

Institut Pasteur

Jeremy Mesple

Institut Curie

Helene Salmon

Institut Curie https://orcid.org/0000-0002-2253-3807

Thierry Rose

Institut Pasteur https://orcid.org/0000-0001-8863-0207

Martine Ben Amar

ENS, Université PSL*, CNRS, Sorbonne Université

Jean Francois Joanny

Curie

Article

Keywords:

Posted Date: July 22nd, 2024

DOI: https://doi.org/10.21203/rs.3.rs-4704301/v1

Additional Declarations: There is **NO** Competing Interest.

Tissue-resident macrophages favor early lung cancer development via direct physical interactions with cancer cells

Jovan Nikolic*[1], Joseph Ackermann*[2,3], Sarah Taheraly[1], François-Xavier Gobert[1], Morgane Mabire[1], Apolline de Folmont[1], Ronan Thibaut[1], Mathieu Morin[1], Ouardia Aït-Mohamed[1], Edison Gerena[4], Sophie Goyard[4,5], Jérémy Mesple[1], Hélène Salmon[1], Thierry Rose[4,5], Martine Ben Amar[2] ✉, Jean-François Joanny[6] ✉, & Philippe Benaroch[1] ✉

1. Institut Curie, PSL* Research University, INSERM U932, Immunity and Cancer, 75005 Paris, France
2. Laboratoire de Physique de l'Ecole normale supérieure, ENS, Université PSL*, CNRS, Sorbonne Université, Université Paris Cité, F-75005 Paris, France
3. Laboratoire Jean Perrin, Sorbonne Université, 4 Place Jussieu, 75005 Paris, France
4. Sorbonne Université, CNRS, Institut des Systèmes Intelligents et de Robotique, 75005 Paris, France.
5. Institut Pasteur, Université de Paris Cité, INSERM-U1224, Cell Biology of Lymphocytes, F-75015 Paris, France
6. Institut Pasteur, Université de Paris Cité, Diagnostic Test Innovation & Development Core Facility, F-75015 Paris, France
7. Institut Curie/Collège de France, 11 place Marcelin Berthelot 75231 Paris Cedex 05, France

* co-first authors.

Address correspondence to:
Jean-François Joanny -jean-francois.joanny@curie.fr
Martine Ben Amar – martine.benamar@phys.ens.fr
Philippe Benaroch - philippe.benaroch@curie.fr

Abstract

While extensive research has unraveled diverse biochemical mechanisms underlying the pro-tumorigenic activities of macrophages, the role of physical forces in early tumor development remains elusive. Here, we integrated experimental data with physical modeling to investigate the contribution of various physical forces. Monitoring the growth of *Kras*^{G12D}*p53*-/- (KP) lung tumor spheroids in vitro in 3 dimensions using real-time microscopy accurately reflects the role of tissue-resident macrophages, rather than monocytes, in promoting tumor growth. Based on the quantitative data, we develop a physical model of 3D spheroid growth to simulate the dynamics of proliferating cancer cells and interacting macrophages, aligning closely with experimental results. When cultured alone, KP lung cancer cells form a single aggregate that contracts over time due to limited nutrient access at the center. The introduction of macrophages promotes the nucleation of cancer cells into multiple small aggregates, which grow before fusing to form a large final aggregate. Throughout this process, macrophages facilitate nutrient access and thus favoring cell division. The theory predicts that adhesion forces between tumor cells and macrophages are essential for the observed tumorigenic effect. Among integrins potentially involved, CD11c is expressed by alveolar macrophages but not by monocytes. Blocking CD11c reduces adhesion forces, preventing spheroid nucleation by macrophages, and impairing growth. Additionally, our theory predicts the redistribution of macrophages towards the periphery of tumor aggregates over time, an evolutionary pattern that we validated in mice *in vivo*. These findings underscore the significant contribution of physical interactions via CD11c between tissue-resident macrophages and cancer cells in the pro-tumor effect of macrophages. Targeting this interaction could offer a new therapeutic strategy to impede early tumor development and metastasis.

Introduction

Single-cell technologies have established that tumor-associated macrophages (TAMs) are very heterogeneous across and within tumors. Two ontogenically distinct populations, i.e. tissue-resident macrophages and monocyte-derived macrophages, are present and may participate in tumor development at specific stages[1,2]. We previously showed that tissue-resident alveolar macrophages (AMØ) are recruited early during tumor initiation in human non-small cell lung carcinoma (NSCLC) as well as in orthotopic and genetically engineered mouse $Kras^{G12D}$ $p53^{-/-}$ (KP) NSCLC models. *In vivo* depletion of $CD169^{+}$ macrophages prior to KP cell injection leads to a substantial reduction in both the number and mass of lung tumor, underscoring the critical role of tissue-resident AMØ to the early stages of lung tumor formation[3]. Notably, depletion of $CD169^{+}$ macrophages once KP tumors are established had no impact on tumor growth. The initial contribution of tissue-resident macrophages at the tumor onset, followed by the recruitment of monocytes, further appears to be a relevant scenario for other types of solid tumors, such as pancreatic adenocarcinoma lesions[4,5].

Neoplastic cells establish complex networks of physical and biochemical interactions with their microenvironment. Early studies pioneered the development of spheroids, aggregates consisting of a single type of cancer cells cultured over various periods, serving as *in vitro* models mimicking tumor biogenesis[6]. Over time, cell adhesion and activity generate a surface tension in the tissue that, coupled with cell proliferation, shapes the aggregate into a spheroid. Furthermore, three-dimensional multicellular spheroids closely mirror the physiological gradients within solid tumors[7]. Cells at the periphery have better access to essential factors such as oxygen or growth factors, and experience less mechanical stress than those at the center. Consequently, edge cells proliferate, while central cells form an apoptotic core, a scenario also observed *in vivo* in nascent, non-vascularized tumors [8–10]. The diffusion of oxygen, growth factors and nutrients, along with mechanical stresses, impose constraints on the size of spheroids and early tumors [11,12].

Theoretical descriptions and numerical studies of tumor spheroids are an active area of research, which aims at exploring quantitatively their growth and structure. One or multiple cell species can be considered[13,14], and the framework of the theory can be discrete or continuous. But, a continuous viewpoint is more adapted to a description of the tumor micro-environment and to the introduction of chemical processes[15,16]. Theoretical and numerical studies are promising in testing quantitatively different scenarios to explain experimental data[17–19]. Simple hypotheses on the structure of the cell-cell interactions give key information on the evolution of the cell aggregates.

In a previous work, we cultured spheroids of KP cells with freshly purified mouse AMØ or monocytes in ultra-low binding plates[3]. RNA sequencing analysis revealed that KP tumor cells co-cultured in 3D spheroids with AMØ, but not monocytes, displayed a transcriptional signature indicative of epithelial-to-mesenchymal transition (EMT), suggesting a potential role for progression toward metastasis. Moreover, while monocytes directly induce proliferation

of KP cells[3], macrophage physical interactions with tumor cells may rather play a crucial role in tumor organization, thereby impacting pro-tumoral activity.

We start with the idea that physical forces may contribute to the initial development of tumor nests, but assessing this question using conventional cell biology approaches is challenging. Our theoretical description offers means to integrate multiple parameters and reasonable approximations in order to build up numerical simulations and to make quantitative predictions, that we compare to our experiments. In this study, we investigated the role of physical forces by initially monitoring the three-dimensional growth of KP tumor spheroids in vitro in the presence of AMØ, observing a positive impact on tumor growth as observed in vivo in early tumor development[3]. We then devised a novel physical description of spheroid growth under various conditions to compare to the experimental findings. This involved constructing an aggregate-based model that considers multiple cell species and accounts for their interactions. We applied this framework to cell aggregates following the lines of Ackermann et al.[15].

Additionally, we employed an individual cell-based model to explore the spatial distribution of cancer cells and AMØs within a spheroid containing both cell types. According to the physical model, interaction forces between macrophages and tumor cells are crucial for the positive effect of AMØs on KP spheroid growth. Inspired by our theoretical predictions, we identified the integrin CD11c expressed by macrophages as a critical molecule for adhesion to KP cells. We further demonstrated that CD11c blockade indeed reverses the positive effect on spheroid growth.

Results

Alveolar macrophages positively impact tumor spheroid growth

We developed a minimal 3-dimensional co-culture of tumor and myeloid cells to quantify the impact of myeloid cells on early lung tumor growth. KP-GFP cells, a mouse NSCLC cell line carrying *Kras* mutation and *p53* deletion, and expressing GFP, were seeded in ultra-low binding plates in the presence of either AMØ purified from bronchoalveolar lavages, bone marrow monocytes (BM-Mo), or none. Fluorescent tumor spheroid growth was monitored over 7 days using time-lapse microscopy. When KP-GFP cells were cultured alone, they quickly adhered to each other, and aggregated into a single spheroid per well. Their sizes ceased to grow after a few hours, and their diameter gradually decreased (Fig. 1A to C, yellow curves and Supplementary video 1). The addition of increasing numbers of AMØs, but not BM-Mo, at day 0, led to a large number of cell clusters, detected as green objects in Fig. 1A and B and in Supplementary video 2. To estimate the tumor spheroid volume, we analyzed images and calculated the projected area of the spheroids, considering either the total area of all GFP^+ objects or the area of the largest GFP^+ object. While addition of AMØs led to an increase in the total spheroid volume, BM-Mo had a minimal impact on the area of GFP^+ objects (Fig. 1A and C, Supplementary video 3). Our findings indicate that the pro-tumorigenic effect of macrophages is specifically recapitulated with AMØ but not with monocytes, highlighting their distinct roles. In conclusion, primary tissue-resident macrophages promote spheroid nucleation and tumor growth compared to monocytes obtained from bone marrow.

Alveolar macrophages impact the spatial organization of the tumor spheroid

To further quantify the impact of AMØ on tumor growth, we performed 3D image analyses of spheroids. Spheroids were retrieved, stained, subjected to clearing with a home-made Trapoïd device (Supplementary Fig. 1C), and imaged by confocal microscopy (Fig. 2A). Three-dimensional reconstruction of the images followed by image analysis revealed that spheroid volume decreases between Day 3 and 7 when KP cells are grown alone (Fig. 2B). The addition of AMØ led to decreased sphericity, accompanied by increased elongation and flatness on Day 3, which was reflected on Day 7 by larger spheroid volumes (Fig. 2B to E). The KP+AMØ object was initially rather elongated (on day 3), potentially due to the coalescence events of the aggregates, but reached a spherical shape over time (on day 7). These observations are correlated to the total number of KP cells between day 3 and 7; they decrease in the condition of KP cells alone while they do not in the presence of AMØ (Fig. 2F).

To identify proliferating cells, we added a deoxynucleotide analog named EdU to spheroid cultures, which can be detected by click chemistry. The proportion of proliferating KP cells was twice as high on Day 3 in the presence of AMØ compared to their absence (4% to 2%), but similar on Day 7 (Fig. 2G). However, these low numbers likely result from the spheroid imaging approach used, which involves collecting the spheroids in the Trapoïd device to undergo the staining/clearing/washes protocol. This likely leads to the selection of the largest objects and the loss of all smaller cell aggregates. Therefore, we repeated the experiment and

collected all the cells present in 12 wells per condition, analyzing them by FACS for KI67 expression (Supplementary Fig. 1A). On Day 3, more than 40% of the KP cells were KI67+ in the presence of AMØ compared to 8% in their absence, with almost no difference on Day 7. This suggests that the addition of AMØ allows KP cells to nucleate and proliferate in multiple aggregates, but this effect is lost upon coalescence into a single large object, as observed on Day 7.

Analysis of the 3D reconstructions of large spheroids revealed that the total number of AMØs associated with spheroids was variable, low, and not significantly different between days 3 and 7, whereas the number of proliferating AMØs decreased over time (Fig. 2H).

To study the spatial distribution of cells, we divided each spheroid into 3 concentric zones of equal volume (edge, intermediate, and core) (Fig. 2I). KP cells were more concentrated in the core than the edge at both times and independently of the presence of AMØ (Fig. 2J and K). AMØs were present in similar proportions in the 3 zones of the spheroids, and their repartition did not change over time (Fig. 2L). In the absence of AMØ, around 70% of proliferating KP cells were located at the edge on days 3 and 7 (Fig. 2M and N). The addition of AMØ distributed proliferating KP cells in the 3 zones in similar proportions, but this effect was largely lost by day 7, with more cells on the edge (Fig. 2K).

We conclude that, at the start of culture, AMØs promote the formation of small cellular aggregates by binding to KP cells. Over time, these aggregates tend to coalesce into a single large object containing a small and variable number of AMØs, with the majority of AMØs likely being excluded from the aggregates.

Physical model of tumor spheroid evolution

In order to understand the mechanism by which AMØs impact tumor spheroid growth, we set up a minimal semi-continuous physical model to treat interactions between proliferating cells. The details are provided in the Supplemental information and summarized in Supplementary Fig. 3A. We focus on the essential physical phenomena with a minimal number of parameters. The values of the parameters are inferred from our experimental data or from existing data in the literature and are displayed in the Supplementary information, Table 1. Our approach is an extended version of the classical Smoluchowski theory for aggregation[20]. We add a spatial component by considering the motion of discrete growing aggregates. Each isolated cell or aggregate moves under the action of external forces and the aggregates have a finite probability to coalesce upon contact. The growth and the shrinkage of an aggregate depend on the mechanical force balance and on the gradient of nutrient concentration inside the aggregate.

An important ingredient of the theory is the distribution of AMØs inside the aggregate. AMØs significantly modify the sedimentation of the aggregates on the surface of the well and must be at least partially localized on the aggregate surface. However, our measurements only detect very few AMØs on the aggregate surface. We conjecture that AMØs remain on the well surface when the aggregates are extracted for measurement or that AMØs are lost during the clearing process. The measurements nonetheless show that AMØs are only present in low

numbers inside the aggregate (Fig. 2H). In addition, no aggregates of AMØs were observed, indicating that they only weakly interact with each other.

We first performed independent particle-based simulations where the interactions are consistent with the experiments. KP cells strongly adhere to each other, they weakly adhere to AMØs, and AMØs do not adhere to each other. With our hypotheses, these simulations indicate that AMØs are located on the surfaces of the aggregates as shown in Supplementary Fig. 2B to D.

In the semi-continuous simulations, we therefore assume that in an aggregate, all AMØs are located on the surface, discarding the very few AMØs still present in the interior of the aggregates. We consider each aggregate as a sphere of radius R and volume V moving at of velocity v . Newton's law imposes that the total external force acting on an aggregate vanishes since inertia is negligible. We only briefly review here the relevant forces, and more details are found in the supplemental information. The buoyancy force is $F_g = -V\Delta\rho g e_z$ where $\Delta\rho$ is the density difference between the spheroids and the medium, g is the gravity acceleration, and e_z is the upward z unit vector. The friction force has two components, parallel and perpendicular to the substrate, which include the Stokes drag force acting on a sphere in a liquid near a container wall, as well as a dependency on the adhesion between the cells and the wall. We also introduce a Langevin random force with a bulk component due to the thermal and active noises and a surface component originating from the active motion of the cells on the walls. A reaction force prevents the penetration of the cell aggregate inside the wall.

When two aggregates or cells (KP or KP-AMØ) are in contact, they merge with a finite probability, but only after maturation of the adhesion between KP cells at contact. They then reorganize to form a single spheroid. The fusion is represented by a Kramer's escape process with probability $p_f = \tau_f^{-1} e^{-\Delta E}$ where τ_f is the fusion timescale. The total energy barrier ΔE depends mostly on the surface density of AMØs and KP cells in both aggregates. It is the sum of two energy barriers:the two layers of AMØs repel each other, and there exists an energy barrier for the adhesion between KP cells and AMØs. After the latency period due to the remodeling of the shape, the new aggregate becomes a spheroid with a volume equal to the sum of the volumes of the merging aggregates. The availability of nutrients limits the growth. A detailed treatment of the diffusion-adsorption of nutrients as well as of themechanical forces is given in the supplementary information following [17]. Finally, we also take into account the adhesion of AMØs to the surface of the well which slows down their motion along the well and thus their sedimentation and that of the aggregates covered by macrophages.

We first study the KP cell proliferation dynamics in the absence of AMØs, and then in the presence of AMØs in the well. The results are compared to the experimental data.

Comparison between numerical and experimental results

The experimental curves obtained by seeding different numbers of KP cells in wells (in the absence of AMØs) are compared to the results of the physical model in Fig. 3A to C. The

time variation of the following variables is studied: number and total area of the aggregates per well, and area of the largest aggregate. We obtain a good agreement for all the variables. The calculated number of KP cells forming the largest aggregate as a function of time with increasing numbers of KP cells initially seeded (Fig. 3D) is compatible with the experimentally measured cell numbers at 72 h and 168 h (Fig. 3D, the two red points with their standard error). These two measurements were achieved after clearing the spheroids and 3D reconstructions as explained in Supplementary Fig. 1C and D and Fig. 2F.3D images of the simulation at different times are shown in Fig. 3E, as well as the 2D projected profile on the XY plane (Fig. 3F) and the evolution of the size of the central aggregate (Fig. 3G). These numerical results are consistent with the experimental observation that the volume of the spheroids decreases with time after the initial coalescence of the small aggregates.

In the presence of both macrophages and KP cells, introduced simultaneously in the wells, tiny aggregates of KP-AMØ are first observed and ultimately coalesce into a large aggregate. To investigate the mechanism of action of AMØs within the spheroids and to calibrate the physical model, we varied the number of AMØs added at the initial time t=0. When the number of AMØs increases from 0 to 5000 cells/well in wells containing initially 2500 KP cells, stronger effects on spheroid nucleation and growth are observed (Fig. 4, shaded curves). As detailed in the previous section, in the absence of AMØs (Fig. 4A to C, yellow curves), tumor cells rapidly form a unique mass of cells that rapidly stops growing. In contrast, the number of tumor nucleation germs increases with the number of AMØs added. The obtained numerical results (curves with vertical bars) compared to the experimental curves (curves with shaded surfaces representing standard errors) give similar profiles for the three variables measured as a function of time: number and total area of aggregates per well, and area of the largest aggregate (Fig. 4A to C). Here also, the estimation by microscopy of the number of KP cells present inside the spheroids at two-time points after clearing and 3D reconstruction (Fig. 4D, two red points at day 3 and day 7 with their standard error) is in agreement with the theory (Fig. 4D). Simulations in 3D from 0 to 7 days in the presence of AMØs are consistent with the observations made by time-lapse microscopy (Fig. 4E, Supplementary video 4):we observe many small cell aggregates in the initial stages, which coalesce to form a single large aggregate at long times. Projection of the simulations in 2D reveals similar features of spheroid growth and AMØ adhesion (Fig. 4F, to compare with Fig 1A).

We conclude that overall, the simulations obtained with our physical approach fit well with the experimental data. The physical model also allows to estimate various parameters presented in Supplementary information Table 1.

CD11c blockade abrogates the positive effect of macrophage on tumor spheroid growth

Our theoretical model predicts that any change in the adhesion forces between AMØs and KP cells should strongly impact the organization and growth of the tumor spheroids.A decrease in these adhesion forces should ultimately abolish the positive effects of AMØs on

tumor spheroid growth (see the numerical results from the simulation for the numbers of aggregates and the total area of the objects in Fig. 5A and B). We, therefore, looked for molecules likely to be involved in the adhesion between AMØs and KP cells. We targeted candidate molecules expressed by AMØs but not monocytes and focused on the family of integrins that are critical in cell-to-cell adhesion processes. The *Itgax* gene that encodes for the protein CD11c satisfied our criteria since it was highly expressed in AMØs at the mRNA level but absent in monocytes (Fig. 5C). This was confirmed at the protein level by flow cytometry (Fig. 5D). To evaluate the contribution of CD11c to the adhesion of AMØs to KP cells, we measured the rupture force of interaction between of KP cells and AMØs in a microscope laminar flow chamber. A laminar shear flow rate was applied to generate drag forces from 0 to 8 nN on individual cells, with an increasing rate of 34 pN/s. AMØs interacting with immobilized KP cells were stretched by this drag force until the rupture of the contact and release of the AMØs into the stream (Supplementary video 5). KP cell- AMØ rupture forces ranged from 0.4 to 8 nN, with half the values between 2.9 and 6.7 nN, suggesting a large variety of cell-to-cell contact formation kinetics or complexity (Fig. 5E). The median rupture force is 4.88 nN. In the presence of an anti-CD11c antibody, the median rupture forceis 3.8, 2.2, 1.5, 1.4, and 1.4 nN for concentrations of 0.01, 0.1, 1, 2, and 5 μg/mL, respectively (Fig. 5E).The median rupture force reached a plateau beyond 1 μg/mL, (see also Supplementary video 6). The presence of isotype control antibody (1 μg/mL) did not perturb the macrophage adhesion as observed with a median rupture force at 4.9 nN, similar to values in the absence of antibodies 4.8 nN.

We then analyzed the effect of the blockade of the integrin αX with the anti-CD11c mAb on the adhesion rate of macrophages added at the time of observation to KP cells adhered to a glass surface for 48 hours. A macrophage is grabbed by a single optical tweezer and brought to a KP cell border. It is dragged along the KP cell surface with a force lower than 100 pN until the macrophage adheres and the 100 pN force is no longer sufficient to move it (Fig. 5F, Supplementary Fig. 4 and Supplementary video 7). The median rolling distance was 18 μm in 2.5 s until the macrophage adhesion to KP cells was stronger than the tweezer force. In the presence of anti-CD11c, this distance and time were dramatically increased with a median rolling time of 26 s and a covered distance of 190 μm. (Fig. 5F, Supplementary Fig. 5 and Supplementary video 8).

Finally, we tested the impact of the same monoclonal antibody (mAb) specific for CD11c against an isotype control in the spheroid tumor growth assay. The addition of the CD11c-specific mAb to the culture abrogated in large parts the positive effect of AMØ on KP spheroid growth in a dose-dependent manner, while the addition of the isotype control had no impact on the evolution of the spheroids (Fig. 5G). We concluded that the adhesion forces exerted via CD11c by AMØs on KP cells were responsible for the positive impact on spheroid growth.

Analysis of KP lung tumor formation in vivo confirms the redistribution of AMØ at the periphery along with tumor development

One prediction of the physical model is that after the merging of the cell aggregates due to the interaction between AMØ and KP cells into a larger structure, AMØ should move forwards the outer edge of the tumor mass. To examine this idea, we injected KP-Luc cells *i.v.* into C57BL/6 mice. Analysis of their lungs tissue post-staining with hematoxylin and eosin staining along with CD11c immunostaining revealed the presence of small tumor foci containing randomly distributed CD11c+ cells (supplementary Fig. 6A). In the peritumoral areas, individual CD11c+ cells were observed, as expected, associated with alveoli. By day 14, the distribution pattern of CD11c+ cells underwent a significant shift (supplementary Fig. 6B). The tumor foci had enlarged considerably, and the majority of CD11c+ cells were now at the immediate periphery of the tumor mass.

Our findings confirm that the physical model's prediction regarding the redistribution of AMØ is indeed observable in vivo during the establishment and progression of KP tumors in the lung.

Macrophages expressing CD11c in contact with tumor cells are observed in human NSCLC lesions

To validate the applicability of our findings to human contexts, we analyzed resected tumors from NSCLC patients using immunohistochemistry (IHC). Formalin-fixed paraffin-embedded (FFPE) sections of previously untreated NSCLC tumor lesions were stained for specific markers of macrophages (CD68), tumor cells (keratin), and CD11c (supplementary Fig. 7). Analysis of overlayed images revealed numerous examples of $CD11c^+$ $CD68^+$ macrophages in direct contact with $keratin^+$ tumor cells. This observation suggests that the interaction of CD11c+ macrophages with tumor cells may play a role in promoting early tumor development in human lung neoplasia.

Discussion

Several studies have documented that during early tumor development, prior to vascularization, tumor cells establish associations with tissue-resident macrophages [3,21–23]. To explore the physical role of tissue-resident macrophages in early tumor development, we conducted a comprehensive experimental and theoretical investigation into the positive impact of tissue-resident macrophages on early lung carcinoma growth. Our rationale was to construct a physical model based on our experimental data and simple hypotheses regarding cell interactions, aiming to provide critical insights into the dynamics of cell aggregates and potentially early tumor development.

We employed a simple *in vitro* model to replicate tumor development, utilizing the mouse NSCLC KP cell line co-cultured without or with freshly isolated AMØs or bone marrow monocytes, in ultra-low-binding plates. Over several days of video monitoring, we observed distinct behaviors of the KP cells under different conditions. When cultured alone, KP cells rapidly formed a single spheroid that compacted and shrank over time. This suggests that after the initial binding of KP cells, adhesive structures tightened between the cells, resulting in a reduction in spheroid volume. In contrast, upon the addition of AMØs at the initial culture stage, but not monocytes, we observed the induction of nucleation of KP cells into multiple aggregates. These aggregates grew and subsequently fused into a single aggregate. This macrophage-induced nucleation led to an increase in the total number of KP cells in the spheroids.

Based on these experimental results, we developed a theoretical model to elucidate the dynamics of spheroids containing both macrophages and cancer cells, aiming to identify the primary factors governing spheroid growth and potentially early tumor growth. The core components of the physical model are the interaction parameters between the different cell types. The physical modeling allows to validate the scenario that macrophages indirectly enhance nutrients access to cancer cells and thereby their proliferation, quantitatively agrees with experimental data.

The theoretical framework progresses in two key steps. Firstly, we apply an individual cell-based model to cell mixtures containing differential cell adhesion. We also consider that spheroid growth is governed by the diffusion of nutrients within the aggregates. The theory assesses the structure of the spheroids and their growth kinetics, leading to two significant findings: i) There is a sparse presence of macrophages within the bulk of the spheroids, with all macrophages primarily located on the surface. ii) Proliferation is notably more pronounced in smaller spheroids due to the accessibility of nutrients to all cells.

In a second step, these theoretical predictions are implemented in an aggregation theory to quantitatively analyze spheroid growth, originating from both pure cancer cell populations and mixtures of cancer cells and macrophages. In the absence of macrophages, we demonstrate the formation of a single large spheroid that grows and eventually saturates at a finite size. Conversely, in the presence of macrophages, numerous small spheroids are initially generated, indicating that macrophages stimulate rapid nucleation of small spheroids, which subsequently fuse to generate larger aggregates.

The essential prediction of the theory is that the final aggregates harbor a larger number of cancer cells in the presence of macrophages. This outcome is attributed to heightened proliferation facilitated by enhanced access to nutrients within the small spheroids, which later fuse to form larger aggregates.

The physical model integrates classical theories of aggregation and tumor growth, effectively reproducing the experimental geometry, the behavior of various cell types, and the structures of aggregates. The parameters derived from our physical model, given in the Supplemental Information Table 1, are in agreement with values previously found in the literature (see supplemental information), comforting the significance of our numerical study.

The physical model offers the following interpretation of the experiments: tumor cell proliferation is influenced by two primary factors: access to nutrients and mechanical stress exerted on the cells [24]. These effects are more favorable when the surface-to-volume ratio of the aggregate is larger. Consequently, smaller aggregates exhibit greater growth compared to larger aggregates, as all their internal cells can undergo division.

When only KP cancer cells are present in the well, the formation of a single aggregate is driven by two distinct features. Firstly, KP cells lack adhesion to the well, causing them to sediment at the bottom of the well within the first hour. There, they stack and coalesce into a unique aggregate. Secondly, KP cells do not immediately adhere to each other upon contact. In general, the compaction of multicellular spheroids occurs in two stages: initially, integrin-ECM bonds form, followed by the accumulation of integrin proteins on the cell surfaces. Both stages are encompassed in a process ofadhesion maturation, which delays spheroid formation [25,26]. When two spheroids merge, their contact zone also undergoes maturation prior to adhesion. Stack formation occurs during this maturation period (Supplementary Fig. 2A).

The introduction of AMØs disrupts both processes. Initially, AMØs adhere to the well, slowing down their sedimentation due to the adhesion-induced friction between the AMØs and the wall. Moreover, AMØs adhere to KP cancer cells over a timescale of minutes. Consequently, small aggregates composed of KP cells and AMØs form rapidly and sediment slowly to the bottom of the well. There, they merge to create a large aggregate. This combined process of aggregation and growth stimulates cancer cell proliferation by the macrophages. Eventually, owing to differences in adhesion between KP cells and AMØs, most AMØs accumulate outside the aggregates, while a minority remains contained within the spheroids, evenly distributed throughout them (Fig. 2H and L), see also Supplementary Fig. 8.

Importantly, validating the physical model's prediction, we observed a similar scenario *in vivo* in the lungs of mice intravenously injected with KP cells. Examination of the lungs on day 7 post-injection revealed small tumor foci containing evenly distributed CD11c+ cells. By day 14, the tumor foci had expanded, with nearly all CD11c+ cells located at the periphery of the tumor mass, with few exceptions noted. While CD11c is also expressed by dendritic cells, AMØ emerge as the predominant cell population expressing CD11c in the lung [27].

The presence of CD11c+ macrophages in proximity to tumor cells in human NSCLC lesions suggests that this phenomenon extends to solid tumors in humans. The spatial

distribution of the tissue-resident macrophages recruited in developing tumors appears of importance for the outcome of their development, a trend observed across various tumor types [3,28,29]. Ultimately, we provide a physical rationale for the observed redistribution of tissue-resident macrophages during tumor development.

Recently, there has been a proposal to incorporate the cell history into the classification of myeloid cell subsets within the TME, alongside their ontogeny and polarization state [30]. Pre-existing tumor-associated macrophages (preTAMs) can be considered as tissue-resident macrophages already dedicated to facilitating the initial stages of tumor development. In this context, AMØ may transition into preTAMs early in the process, aiding circulating tumor cells in establishing niches within the alveoli by virtue of their ability to physically interact with them via CD11c.

Our key finding is that enhanced KP cell proliferation in the experiments may arise from the nucleation of multiple aggregates by macrophages, facilitating nutrient access for cancer cells without inducing biochemical changes in their proliferation properties. Our *in vitro* experimental findings highlight the critical role of adhesion forces and, notably, the adhesion kinetics between tissue-resident macrophages and KP cancer cells, which greatly depends on the CD11c integrin—a molecule expressed at low levels by monocytes. Blocking CD11c engagement with a specific antibody led to a significant decrease in forces and adhesion rates, as well as the elimination of the positive effect induced by macrophages on spheroid growth. Thus, the results of CD11c blockade suggest that soluble factor(s) may not play a role in the macrophage effect, although this possibility cannot be entirely excluded.

The presence of an anti-CD11c blocking antibody did not entirely prevent macrophage binding to KP cells, suggesting the involvement of other receptors. CD11c, the αX chain integrin, is a member of the β2 integrin family and is known to associate with CD18 to form the heterodimer αXβ2. This integrin exhibits promiscuity, serving as a receptor for various molecules such as the complement C3 cleavage product iC3b [31], fibrinogen [32], denatured proteins [33], and intercellular adhesion molecule (ICAM)-1 [34]. While other integrins expressed by macrophages, such as β4, have been reported to be crucial for macrophage adhesion and lympho-vascular remodeling that favors metastasis [35], there is currently no reported evidence of similar activities for CD11c.

The diameter of spheroids on Day 7 ranged from approximately 200 µm in the absence of macrophages to 300 µm in their presence. Despite the irregularity of blood vessels in tumors, the typical distance between two vessels is on the order of a hundred micrometers, consistent with nutrient consumption patterns such as oxygen or glucose molecules [36,37]. These dimensions correspond to spheroid sizes, with their centers positioned at 100 to 150 µm from the surface, rendering them vulnerable to hypoxia and nutrient deficiencies. As tumor development progresses to later stages, the applicability of our model diminishes due to the complex interactions among diverse cell and protein components within the tumor microenvironment (TME). This holds true at the experimental level, where spheroids can mimic tumor development before recruitment of monocytes and vascularization. However,

focusing on early tumor formation provides an opportunity to explore the integration of additional cell populations within the TME, such as fibroblasts or subpopulations of macrophages with different phenotypes.

Our study offers a novel insight into the relationship between cancer progression and macrophage-induced nucleation of aggregates, expanding on previous observations correlating trans-coelomic metastasis with macrophage-induced spheroid formation [38].

Our research raises several intriguing questions that warrant further investigation. These include exploring the consequences of macrophage clustering cancer cells on tumor heterogeneity and evolution, as well as investigating the implications on spatial organization and resistance to attack from tumor-specific T cells.

The physical interaction mediated by CD11c between AMØs and tumor cells represents a promising druggable target. Treatments with CD11c agonists could potentially impede early tumor or metastasis development in cancer patients across various contexts. Disrupting the tight physical interaction between tissue-resident macrophages and tumor cells could therefore serve as an adjuvant treatment strategy across different tumor types to prevent the establishment of metastasis.

Acknowledgements

We thank Drs Ana-Maria Lennon-Dumenil, Jason Cosgrove and Maria Casanova Acebes for fruitful discussions and critical reading of the manuscript. We thank Dr Isabelle Puisieux for her help in the analysis of tissue sections. This work was supported by grants from Laboratoire d'Excellence (Labex) DCBIOL (ANR-10-IDEX-0001-02 PSL and ANR-11-LABX-0043), PSL-maturation-Qlife, Curie Innov' to P.B.. The grants ITMO PCSI and ITMO MCMP were attributed to PB, JFJ, MB and HS. PB also benefited from a grant "Chercher trouver" shared with HS. ATF was supported by fellowship from the ARC (association de recherche contre le cancer). MM and RT were supported by ITMO MCMP and AdF by a fellowship from Ligue de la recherche contre le cancer. JA and MBA acknowledge the support of ANR (Agence Nationale de la Recherche) under the contract MecaTiss (ANR-17-CE30-0007) and the contract Epi-Morph (ANR-18-CE13-0008). JA acknowledges the financial support from ANR COLLAMOEBOID (ANR-20-CE13-0031).

Author Contributions

JN and PB designed and supervised the biological experimental research. MBA and J-FJ supervised the theoretical physic research. JN performed most of the experiments with the technical help of ST, and built the Figs. JA, MBA and J-FJ set up the physical model, run simulations and wrote the supplemental information. MM wrote the ImageJ program to analyze the images. F-XG designed the Trapoïd device. AF, RT, JN performed mouse experiments. MM, JM and HS performed IHC staining

and analysis. TR, SG and EG performed the force assays, which were analyzed by TR. OAM performed the heatmap analysis. PB, JN, J-FJ, JA, MBA wrote the paper. HS edited the paper.

References

1. Christofides, A. *et al.* The complex role of tumor-infiltrating macrophages. *Nat. Immunol.* **23**, 1148–1156 (2022).
2. Park, M. D., Silvin, A., Ginhoux, F. & Merad, M. Macrophages in health and disease. *Cell* **185**, 4259–4279 (2022).
3. Casanova-Acebes, M. *et al.* Tissue-resident macrophages provide a pro-tumorigenic niche to early NSCLC cells. *Nature* **595**, 578–584 (2021).
4. Zhu, Y. *et al.* Tissue-Resident Macrophages in Pancreatic Ductal Adenocarcinoma Originate from Embryonic Hematopoiesis and Promote Tumor Progression. *Immunity* **47**, 323-338.e6 (2017).
5. Baer, J. M. *et al.* Pancreas resident macrophage-induced fibrosis has divergent roles in pancreas inflammatory injury and PDAC. 2022.02.09.479745 Preprint at https://doi.org/10.1101/2022.02.09.479745 (2022).
6. Sutherland, R. M., McCredie, J. A. & Inch, W. R. Growth of multicell spheroids in tissue culture as a model of nodular carcinomas. *J. Natl. Cancer Inst.* **46**, 113–120 (1971).
7. Hirschhaeuser, F. *et al.* Multicellular tumor spheroids: an underestimated tool is catching up again. *J. Biotechnol.* **148**, 3–15 (2010).
8. Tannock, I. F. The relation between cell proliferation and the vascular system in a transplanted mouse mammary tumour. *Br. J. Cancer* **22**, 258–273 (1968).
9. Bennington, J. L. Cellular kinetics of invasive squamous carcinoma of the human cervix. *Cancer Res.* **29**, 1082–1088 (1969).
10. Yamamoto, A. *et al.* Metastasis from the tumor interior and necrotic core formation are regulated by breast cancer-derived angiopoietin-like 7. *Proc. Natl. Acad. Sci. U. S. A.* **120**, e2214888120 (2023).
11. Cheng, G., Tse, J., Jain, R. K. & Munn, L. L. Micro-environmental mechanical stress controls tumor spheroid size and morphology by suppressing proliferation and inducing apoptosis in cancer cells. *PloS One* **4**, e4632 (2009).
12. Han, S. J., Kwon, S. & Kim, K. S. Challenges of applying multicellular tumor spheroids in preclinical phase. *Cancer Cell Int.* **21**, 152 (2021).
13. Montel, F. *et al.* Stress clamp experiments on multicellular tumor spheroids. *Phys. Rev. Lett.* **107**, 188102 (2011).
14. Van Liedekerke, P. *et al.* Quantitative cell-based model predicts mechanical stress response of growing tumor spheroids over various growth conditions and cell lines. *PLoS Comput. Biol.* **15**, e1006273 (2019).
15. Ackermann, J., Ben Amar, M. & Joanny, J.-F. Multi-cellular aggregates, a model for living matter. *Phys. Rep.* **927**, 1–29 (2021).
16. Ramírez-Torres, A. *et al.* Biomechanic approach of a growing tumor. *Mech. Res. Commun.* **51**, 32–38 (2013).
17. Basan, M., Prost, J., Joanny, J.-F. & Elgeti, J. Dissipative particle dynamics simulations for biological tissues: rheology and competition. *Phys. Biol.* **8**, 026014 (2011).
18. Frieboes, H. B. *et al.* Computer simulation of glioma growth and morphology. *NeuroImage* **37 Suppl 1**, S59-70 (2007).
19. Bearer, E. L. *et al.* Multiparameter computational modeling of tumor invasion. *Cancer Res.* **69**, 4493–4501 (2009).
20. Smoluchowski, M. V. Drei Vortrage uber Diffusion, Brownsche Bewegung und Koagulation von Kolloidteilchen. *Z. Phys.* **17**, 557–585 (1916).
21. Qian, B. *et al.* A Distinct Macrophage Population Mediates Metastatic Breast Cancer Cell Extravasation, Establishment and Growth. *PLOS ONE* **4**, e6562 (2009).
22. Chen, Q., Zhang, X. H.-F. & Massagué, J. Macrophage Binding to Receptor VCAM-1

Transmits Survival Signals in Breast Cancer Cells that Invade the Lungs. *Cancer Cell* **20**, 538–549 (2011).
23. Rodriguez-Tirado, C. *et al.* Interleukin 4 Controls the Pro-Tumoral Role of Macrophages in Mammary Cancer Pulmonary Metastasis in Mice. *Cancers* **14**, 4336 (2022).
24. Ben Amar, M., Nassoy, P. & LeGoff, L. Physics of growing biological tissues: the complex cross-talk between cell activity, growth and resistance. *Philos. Trans. R. Soc. A* **377**, 20180070 (2019).
25. Lee, B. H. *et al.* Modulation of Huh7.5 spheroid formation and functionality using modified PEG-based hydrogels of different stiffness. *PloS One* **10**, e0118123 (2015).
26. Lin, R.-Z., Chou, L.-F., Chien, C.-C. M. & Chang, H.-Y. Dynamic analysis of hepatoma spheroid formation: roles of E-cadherin and beta1-integrin. *Cell Tissue Res.* **324**, 411–422 (2006).
27. Misharin, A. V., Morales-Nebreda, L., Mutlu, G. M., Budinger, G. R. S. & Perlman, H. Flow Cytometric Analysis of Macrophages and Dendritic Cell Subsets in the Mouse Lung. *Am. J. Respir. Cell Mol. Biol.* (2013) doi:10.1165/rcmb.2013-0086MA.
28. Müller, S. *et al.* Single-cell profiling of human gliomas reveals macrophage ontogeny as a basis for regional differences in macrophage activation in the tumor microenvironment. *Genome Biol.* **18**, 234 (2017).
29. Ramos, R. N. *et al.* Tissue-resident FOLR2+ macrophages associate with CD8+ T cell infiltration in human breast cancer. *Cell* **185**, 1189-1207.e25 (2022).
30. Blériot, C., Dunsmore, G., Alonso-Curbelo, D. & Ginhoux, F. A temporal perspective for tumor-associated macrophage identities and functions. *Cancer Cell* **42**, 747–758 (2024).
31. Bilsland, C. A., Diamond, M. S. & Springer, T. A. The leukocyte integrin p150,95 (CD11c/CD18) as a receptor for iC3b. Activation by a heterologous beta subunit and localization of a ligand recognition site to the I domain. *J. Immunol.* **152**, 4582–4589 (1994).
32. Nham, S. U. Characteristics of fibrinogen binding to the domain of CD11c, an alpha subunit of p150,95. *Biochem. Biophys. Res. Commun.* **264**, 630–634 (1999).
33. Davis, G. E. The Mac-1 and p150,95 beta 2 integrins bind denatured proteins to mediate leukocyte cell-substrate adhesion. *Exp. Cell Res.* **200**, 242–252 (1992).
34. Blackford, J., Reid, H. W., Pappin, D. J., Bowers, F. S. & Wilkinson, J. M. A monoclonal antibody, 3/22, to rabbit CD11c which induces homotypic T cell aggregation: evidence that ICAM-1 is a ligand for CD11c/CD18. *Eur. J. Immunol.* **26**, 525–531 (1996).
35. Evans, R. *et al.* Integrin-Mediated Macrophage Adhesion Promotes Lymphovascular Dissemination in Breast Cancer. *Cell Rep.* **27**, 1967-1978.e4 (2019).
36. Freyer, J. P. & Sutherland, R. M. Regulation of growth saturation and development of necrosis in EMT6/Ro multicellular spheroids by the glucose and oxygen supply. *Cancer Res.* **46**, 3504–3512 (1986).
37. Baish, J. Role of Tumor Vascular Architecture in Nutrient and Drug Delivery: An Invasion Percolation-Based Network Model. *Microvasc. Res.* (1996).
38. Long, L. *et al.* Tumor-associated macrophages induced spheroid formation by CCL18-ZEB1-M-CSF feedback loop to promote transcoelomic metastasis of ovarian cancer. *J. Immunother. Cancer* **9**, e003973 (2021).
39. Muzumdar, M. D., Tasic, B., Miyamichi, K., Li, L. & Luo, L. A global double-fluorescent Cre reporter mouse. *genesis* **45**, 593–605 (2007).
40. Dobin, A. *et al.* STAR: ultrafast universal RNA-seq aligner. *Bioinforma. Oxf. Engl.* **29**, 15–21 (2013).
41. Liao, Y., Smyth, G. K. & Shi, W. The Subread aligner: fast, accurate and scalable read mapping by seed-and-vote. *Nucleic Acids Res.* **41**, e108 (2013).
42. Love, M. I., Huber, W. & Anders, S. Moderated estimation of fold change and dispersion for RNA-seq data with DESeq2. *Genome Biol.* **15**, 550 (2014).

43. Gu, Z., Eils, R. & Schlesner, M. Complex heatmaps reveal patterns and correlations in multidimensional genomic data. *Bioinforma. Oxf. Engl.* **32**, 2847–2849 (2016).
44. Hama, H. *et al.* ScaleS: an optical clearing palette for biological imaging. *Nat. Neurosci.* **18**, 1518–1529 (2015).
45. Schindelin, J. *et al.* Fiji: an open-source platform for biological-image analysis. *Nat. Methods* **9**, 676–682 (2012).
46. Edelstein, A. D. *et al.* Advanced methods of microscope control using μManager software. *J. Biol. Methods* **1**, e10 (2014).
47. Schneider, C. A., Rasband, W. S. & Eliceiri, K. W. NIH Image to ImageJ: 25 years of image analysis. *Nat. Methods* **9**, 671–675 (2012).
48. Juzans, M. *et al.* Adenomatous Polyposis Coli Modulates Actin and Microtubule Cytoskeleton at the Immunological Synapse to Tune CTL Functions. *ImmunoHorizons* **4**, 363–381 (2020).
49. Gerena, E. *et al.* Tele-Robotic Platform for Dexterous Optical Single-Cell Manipulation. *Micromachines* **10**, 677 (2019).

Methods

Mice

C57BL/6J female mice of 8–10 weeks old were used for tumour experiments (supplied by Charles River). Mice were maintained at specific-pathogen free (SPF) health status in individually ventilated cages at 21°C and 40–50% humidity, under 12h light–dark cycles. Ethical approval for mouse experiments was obtained by the Comité d'éthique en expérimentation animale from Institut Curie (CEEA-IC#118, DAP2020-022).

Tumor induction in vivo

KP-Luc-DBY cells were grown in complete medium (RPMI + 10% FBS + 1% P/S), and 70% confluent cultures were detached using TryPLE Express (Gibco) and counted. A total of 5 × 10^5 KP-Luc-DBY cells were intravenously injected in 1X phosphate-buffered saline (PBS) into the tail vein and allowed to form tumor foci for 7 to 14 days before the lungs were collected.

Histopathology

Tumor quantification was assessed in paraffin-embedded lung slides stained with haematoxylin and eosin. Slides were scanned using an Olympus Digital Scanner.

Multiplex histological staining

Multiplexed IHC was performed according to the protocol developed by , with some adjustment. Tissues were baked at 60°C for 1h, deparaffinized in Xylene (Fisher Scientific, 10467270) and rehydrated. The heat-induced epitope retrieval was done with pH6.1 citrate buffer (Dako, S169984-2) or pH9 EDTA buffer (Dako, S236784-2) in a 95°C water bath for 30 minutes for the first staining (otherwise 15min) followed by incubation in REAL peroxydase blocking solution (Agilent Dako, S202386-2) for 10 minutes. If the primary antibody was the same species as any antibody used in prior stains, another blocking step was added with Fab Fragment, for anti-rabbit (Jackson ImmunoResearch Europe Ltd, 711-007-003) and anti-mouse (jackson ImmunoResearch Ltd, 715-007-003) for 20 minutes. Protein block serum free (Agilent Dako, X090930-2) was added for 10 minutes. Primary antibody (rabbit anti-human CD11c Abcam ab56632, mouse anti-human CD68 Agilent M081401-2 and mouse anti-human Keratin Agilent M351529-2) was incubated between 1 and 2 hours at room temperature. The primary antibody was detected with a secondary antibody directed against it, conjugated with horseradish peroxydase (Anti-rabbit: Agilent Dako, K400311-2) (Anti-mouse: Agilent Dako, K400111-2) (anti-goat :R&D systems, VC004-050)(Anti-rat : BioTechne, VC005-050) followed by chromogenic revelation with 3-amino-9-ethylcarabazole (AEC) (Agilent Dako, K3468). Slides were counterstained with hematoxylin (Thermo Scientific, 6765001) and mounted with Glycergel aqueous mounting medium (Dako, C056330-2). After scanning (NanoZoomer S360 Digital slide scanner, C13220-04), tissues were bleached with ethanol baths and another cycle was performed starting with the heat induced epitope retrieval.

Histology analysis and overlays

Each IHC staining was deconvoluted with HALO's (indicalab.com) module Deconvolution version 1.1.8. Then, overlays were done according to HALO's guidelines. Histology visualizations were performed using the open-source image analysis QuPath software (QuPath-0.4, https://qupath.github.io/).

Isolation of bronchoalveolar macrophages and purification of bone marrow monocytes

AMØwere isolated by washing the lung of C57BL/6 wild-type mice or mTmG mice expressing membrane-targeted tandem Tomato dimers[39] with 5 x 1ml of MACS Buffer (PBS 1X, 1% FCS, 0,5mM EDTA). Bone marrow monocytes were isolated using a bone marrow monocyte isolation kit (Miltenyi 130-100-629) according to the manufacturer's instructions.

Spheroid formation and time-lapse imaging

KP-GFP cells were grown in complete medium in 96-well round bottom Ultra-Low Attachment microplates (Corning, 7007) to allow spheroid formation. A varying initial number of KP-GFP cells were grown alone or 2500 KP-GFP cells were mixed with varying number of TRMs or bone marrow monocytes for 7 days. When indicated, blocking anti-CD11c antibody (clone N418, eBioscience 15288377) or an isotype control (IgG Armenian Hamster, eBioscience 17151252) were added at the indicated concentration.

Spheroids were imaged with a robotized microscope placed in an incubator (IncuCyte S3, Sartorius). Green fluorescence, red fluorescence and phase contrast images were acquired every 3 h for 7 days. A mask based on the green fluorescence intensity was created to detect the green objects, which are tumor spheroids. The size and the number of the tumors spheroids was quantified using IncuCyte software.

Bulk RNA-seq

RNA isolation was done with the Qiagen RNeasy micro kit. One nanogram of RNA was synthesized into cDNA using the Smart-Seq v4 Ultra Low Input RNA Kit for Sequencing (Takara Bio). Sequencing libraries were prepared using the Low Input Library Prep Kit (Takara Bio). Libraries were sequenced on an Illumina NextSeq 550 System. 75 single-end RNAseq reads were mapped onto the mm10 genome using STAR[39] version 2.7.3a. After the mapping, chimeric reads were removed. Expression levels of individual genes were obtained using featureCounts from Subread[41]version 1.5.1 and transcripts per million (TPM) were calculated for each gene. Differential expression analysis was performed using DESeq2[42]version 1.19.37 on raw read counts to obtain normalized fold changes (FC) and *Padj*-values for each gene. Heatmaps were produced using the R package ComplexHeatmap[43]version 2.8.0.

Flow cytometry

Single-cell suspensions of bronchoalveolar AMØs or bone marrow monocytes were stained in FACS buffer (PBS supplemented with 10% BSA and 2 mM EDTA) with a PE-Cy7 anti-CD11c antibody (Biolegend 117318) and analyzed on a BD FACS Verse.
For spheroids, 12 wells per condition were pooled and dissociated with Accutase (Stemcell technologies) for 20 min at 37 °C and under agitation. Cells were stained in FACS buffer with a BV605 anti-CD45 antibody (Biologend 103140). Cells were fixed with Invitrogen Fix/Perm according to the kit instructions, stained with a AlexaFluor 647 anti-Ki67 antibody (BD 561126) and analyzed on a Novocyte (Agilent).

Spheroid imaging

Spheroid were immobilized in a PDMS device (Trapoïd) enabling histological preparation and observation. The device consists of two chambers connected by a channel of a height smaller than the diameter of the spheroid to be observed (0.15µm). Each chamber at the level of the channel ends in a tip to block the spheroid in place for proper imaging.
PDMS (GE Silicones) was used to prepare the device from a custom-made 3D printed mold. 3D custom made mold was printed on a ELEGOO mars PRO 3D printer with ELEGOO WATER Washable photopolymer resin. Molds were sonicated 3 times in water for 5 min to remove the traces of non-polymerized resin. The PDMS chamber and a 24x60mm microscope cover glass (VWR ECN 631-1575) were plasma activated before being bound to each other. The binding was left to strengthen in a 65°C oven for 1 hour.

Immunofluorescence and imaging

3hours prior fixation 5µM EdU (5-ethynyl-2'-deoxyuridine) was added to spheroid media for labeling dividing cells. Spheroids were collected, washed 3 times with PBS fixed using 4% PFA in PBS for 1hour and transferred into a Trapoïd device. Permeabilization was done using penetration buffer (PBS, 0,2%Triton 100X, 0,3M Glycine, 20%DMSO) for 1hour. Spheroids were washed with wash buffer (PBS, 3% BSA). EdU detection cocktail was added following supplier's instruction. (Click-iT EdU Imaging Kit A647, Invitrogen). Spheroids were washed with wash buffer and incubated with Hoechst® 33342 (Thermofisher) in penetration buffer for 30 min at RT. Spheroids were washed in PBS and cleared using ScaleS4 media (D-Sorbitol 40(w/v)%; Glycerol 10(w/v)%; Urea 4M; DMSO 20(v/v)%) for 48h at 37°C [44].

Of note, the staining of spheroids with EU, another nucleotide analog incorporated into nascent RNA, was homogeneous throughout the spheroids (Supplementary Fig. 1A). Since EdU and EU possess similar structures, it suggests that EdU can also penetrate the whole spheroids.

Imaging was performed using a Leica DMi8 inverted microscope connected to a SP8 scanning confocal unit microscope equipped with four laser diodes (405, 488, 546, and 633 nm) and two hybrid detectors. For all acquisitions, a Leica 40x glycerol immersion objective HCPL APO (NA=1,25) was used and a Z-compensation was applied, modifying the detector gain and the laser intensity to ensure a homogenous signal through the z-stack. Images were acquired with a z-step of 2µm.

Image analysis

Image analysis was performed using Fiji [45]. First, a mask of the total spheroid, the macrophages cell body and the proliferating nucleus was obtained by applying a threshold respectively on the GFP channel, the TdTomato channel and the EdU channel. A gaussian blur (2px radius) was used to remove noise and a fill hole was apply on the macrophages mask to fill entirely their cell body.

3D object counter was use on the spheroid mask to get properties such as volume surface and bounding box and a 3D distance map corresponding to the distance to the edge of the spheroid was obtained from the total spheroid mask using 3D distance map function from imageJ 3D suite (v3.96.4).

ImageJ 3D suite (v3.96.4) was also used to compute 3Dshape parameter of the spheroid. Sphericity is defined as =36π(V2/S3) where V is the Volume and S, the Surface. Elongation and flatness are computed after an ellipsoid fitting. Elongation is calculated by doing as $P^2/(4\pi/A)$ where P is the Perimeter and A, the Area. Regarding the Flatness, it is defined as length of intermediate axis divided by the length of the shortest axis of the object. Compactness is defined as = [sqrt(4 * area / PI)] / [major axis].

To do a cell-by-cell analysis, each nuclei center was detected using the Log detection from Trackmate (radius=10 microns), and a 3D binary image of all nuclei center positions was generated.

For each nucleus position, the distance to the edge was measured on the 3D distance map and the positivity to tdTomato or EDU was measured on the macrophages or proliferating

cell mask. One representative example of the masks obtained is represented in Supplementary Fig. 1C and Supplementary video 9.
To analyze the distance to the edge distribution, the percentage of each cell population in some concentric regions corresponding to 3 equal volumes were measured for all cell populations. Briefly, to define the 3 regions, the distance map was normalized from 0 for the edge to 1 for the center of the spheroid. The 3 volumes were then defined according to those normalized distances, from 0 to 0.126 for the external region, from 0.126 to 0.307 from the intermediate one, and from 0.307 to 1 for the internal region. Those values were chosen to define 3 equal volumes if we approximate the spheroid as a sphere.

Rupture force assay of KP cell-macrophage interactions in laminar flow chamber

Adhesive flow chambers (Slide I0.1, Ibidi, Germany) were assembled on surface-treated cell culture dishes (Startdest) and placed in an oven at 55°C for 30 min. KP cells were grown in RPMI 10% FBS (Lonza) at 37°C, CO2 5% for two days in Petri dishes were resuspended with 2 mL of trypsin-EDTA (Sigma-Aldrich) per dish for 5 min at room temperature. KP cell suspension is diluted with 13 mL of RPMI completed with 10% FBS then centrifuged for 5 min at 1000g. KP cells are resuspended in 1 mL of RPMI with 10% FBS. Ibidi chambers were rinsed with 1mL of RPMI then, filled with 50 uL of KP cell suspension then incubated for 4 hrs at 37°C CO2 5% in a humidified atmosphere. Culture media was then gentled renewed (50uL) and cells were incubated overnight.Culture media was then gentled renewed (50mL) was carefully added, and cells were incubated for 4 hrs at 37°C. Mouse macrophages were stored in RPMI 10% FBS, then centrifuged and resuspended in 200 mL of warm RPMI 10% FBS. In the absence or presence of antibody anti-CD11c (0, 10, 100, 1000 ng/mL final concentration), 50 mL of macrophage suspension was gently loaded in the chamber in the presence of KP cells and then incubated for 10 min at 37 °C. The chamber was connected to a syringe pump (SP210iW, WPI) controlled by a computer. The syringe was filled with RPMI. A flow rate was applied through the chamber for 92 s increasing from 0 to 38.4 mL/min, synchronized with image acquisition (3 image/s, 1100 x 840 µm) using an inverted transmission microscope (Observer D1, Zeiss) with a 10x/0.3 NA objective controlled by MicroManager (Edelstein *et al.*, 2014) .

Image series were analyzed using ImageJ software [47] and the plugin CellCounter. KP cells and macrophages were distinguished from their size and shape. The flow rate value at the cell-cell rupture event was used to compute the dragging force on the released cell according to its size (mean diameter of 12 µm), shape (roughly spherical) and density (mean value 1.20 kg/L). Calibration of dragging force was performed from sedimentation rate of cells in the chamber (RPMI density 1.0034 kg/L and dynamic viscosity 0.6998 mPa.s at 37°C) (35) and the theoretical flow speed *versus* wall distance according to Poiseuille solution to Navier-Stokes formalism for a Reynolds' number below 10 characterizing a laminar flow. Calculus of force from cell size and flow rate have been detailed previously by Rose and colleagues [48] . The number of cells loaded in the chamber and located in the field of view may vary from one experiment to another.

Adhesion assay of macrophages on KP cells using optical tweezers

KP cells were grown on glass bottom Petri dishes (Matek 35mm) in RPMI 10% FBS. In the absence or presence of antibody anti-CD11c (1000mg/mL final concentration) incubated in 50 mL of macrophage suspension was gently loaded in the dish in the presence of KP cells. Cells were then observed using a custom-made inverted transmission microscope with high-speed CMOS camera (Basler, Ahrensburg, Germany, 659 × 494 px) and an oil immersion objective (Olympus UPlanFLN 40x, NA 1.3). For trapping micrometric objects, a near-infrared laser (1070 nm) minimizing phototoxicity is piloted using a 7-degree of freedom joystick actuating high-speed laser-deflection generated by a galvanometer (GVS002, Thorlabs, Newton, NJ, USA) and a deformable mirror (PTT111 DM, Iris AO, Berkeley, CA, USA). The 3D motion of the focal spot is obtained by the synchronization of the orientation of the galvanometer mirror and focusing or defocusing the deformable mirror. A 3D-nano stage is controlled by a piezo motor [49] .The nano-stage moves the Petri dish while trapped macrophages remain fixed. Multiple traps are created by sequentially moving the focal spot between different positions. This time-sharing method is made possible by the short response time of the galvanometer and the deformable mirror, and a real-time control framework implemented on a Real-Time kernel (Xenomai). This design allows the creation of numerous independent optical traps within a volume of approximately 70 × 50 × 9 µm3 with a bandwidth of up to 200 Hz. Tweezer force actuations are limited to 500 pN on macrophages because of the low difference in cell density with the media.

Figure legends

Fig. 1. Evolution of 3D tumor spheroids cultured with alveolar macrophages or monocytes

A. Representative images from movies of 2500 KP-GFP tumor cells co-cultured with 5000 BM-Mo, 5000 AMØ, or alone on days 1, 3, and 7 are shown (extracted from Supplementary video 1 to 3). Myeloid cells were prepared from transgenic mice expressing a membrane-targeted dimer Tomato. The images were acquired over several days with an InCucyte microscope in the GFP and Tomato channels and light transmission. Scale bar = 200µm

B-C. Graphs show the quantifications of the number of aggregates, total area, and largest object area from co-cultures with AMØ or BM-Mo. Images were taken every 3 hours during the first 168 hours of culture. The mean of 3 independent experiments is represented by each colored curve, which corresponds to a different number of AMØ or monocytes.

Fig. 2. Spatial quantification of the evolution of tumor spheroid growth in the presence or absence of alveolar macrophages

A. Representative images of KP-GFP spheroids co-cultured with AMØ or alone on days 3 and 7. EdU was added to the cultures for the last four hours to identify the proliferating cells present in the spheroids. The spheroids were fixed, stained with Hoechst, cleared, and analyzed using confocal microscopy. Complete 3D reconstructions were built using stacks of spheroid images acquired every 2 µm. The XY and ZX median planes are presented here. Scale bar = 100µm.

B-H. Quantifications of the 3D spheroid reconstitutions on days 3 and 7 were performed using algorithms developed in Fiji (see Material and Methods) to achieve cell segmentation and measure the indicated parameters. The sphericity was calculated using the formula $Sph=36\pi V2/S3$, where V is the volume and S is the surface of the aggregate. The results were obtained from three independent experiments, with 10 to 12 spheroids per condition. Unpaired t-test *P≤0.05, **P≤0.01, ***P≤0.001.

I. Spheroid representation in 2D and 3D. Each spheroid was approximated as a sphere and divided into three concentric regions of equal volume.

J-N. Graphs showing the percentage of (**J**-**K**) KP cells, (**M**-**N**) proliferating KP cells and (**L**) AMØ in each region on days 3 and 7.

Fig. 3. Comparison between the experimental data and the 3D simulations of the evolution of KP growth in the absence of macrophages

A-D. The graphs display (**A**) the number of aggregates, (**B**) the total area of GFP+ objects, (**C**) the largest object area and (**D**) the number of KP cells in the largest object over time from 0 to 175h co-culture. The two red points with error bars represent the comparison between simulation and experimental results obtained by confocal imaging quantification of cleared spheroids obtained after seeding of 2500 KP-GFP cells collected at 72h (day 3) and 168h (day 7). Experimental curves are presented with shaded surfaces representing standard errors (N=3 independent experiments). Simulations obtained through mathematical modeling are shown as plain lines with vertical bars indicating standard errors. Each colored curve corresponds to a different number of KP cells seeded at t = 0. The same parameters were applied to the mathematical modeling, which generates some variation upon repeats due to the stochasticity introduced. The results obtained by both approaches are overlaid.

E-F. Representation of KP spheroid surface growth by (**E**) a 3D simulation and (**F**) an XY projection at five different timepoints. **G**. Overlay in 2D of the size of the largest object at three timepoints based on the mathematical modeling.

Fig. 4. Comparison between the experimental data and the simulations in 3D of the evolution of KP growth in the presence of increasing numbers of macrophages

A-D. Graphs showing (**A**) the number of aggregates, (**B**) the total area of GFP+ objects, (**C**) the largest object area and (**D**) the number of KP cells in the largest object over time from 0 to 175h co-culture. Two red dots with error bars represent the experimental results obtained by confocal imaging quantification of cleared spheroids obtained after seeding 2500 KP-GFP cells with 5000 macrophages harvested at 72h (day 3) and 168h (day 7). The experimental curves display shaded areas to represent the standard deviation, while simulations obtained through mathematical modeling are shown as plain lines with vertical bars to indicate the standard error. The experiments involved seeding 2500 KP-GFP tumor cells per well with varying numbers of freshly isolated alveolar macrophages (0, 625, 1250, 2500, and 5000 AMØ). Each colored curve corresponds to a different number of alveolar macrophages initially seeded. During the first 175 hours of culture, images were captured using an IncuCyte and the same parameters were used for mathematical modeling. The results obtained from both approaches are overlaid. **E-F**. The growth of the KP-GFP cells and AMØ spheroid surface is represented in 3D simulation (E) and XY plane projection (F) at five different timepoints.

Fig. 5. Blocking CD11c inhibits the positive impact of alveolar macrophages on tumor growth in vitro.

A-B. Simulations of the evolution of (**A**) the number of aggregates and (**B**) the total area of GFP+ objects when reducing the interaction forces between macrophages and tumor cells.

C. Heat map analysis of RNAseq data obtained from freshly isolated bone marrow monocytes and alveolar macrophages. Here is displayed the TPM for members of the integrin family. N = 3 replicates. The gene *Itgax* encodes for the CD11c protein. **D**. Flow cytometry histogram of the CD11c surface expression in bone marrow monocytes and alveolar macrophages. **E**. Rupture force assay of KP cell-macrophage interactions in a laminar flow chamber in the presence of anti-CD11c at varying concentrations. The left panel shows a whisker-box plot of quartiles of dragging force values at the cell-cell interaction rupture event under the indicated conditions. The right panels show successive images displayed as tiles under the indicated conditions, with the dragging force scale detailed at the top. AMØ were gently loaded onto KP cells seeded in adhesive flow chambers in the presence of the indicated antibodies at various concentrations for 10 minutes and submitted to an increasing flow rate synchronized with image acquisition. The image series were analyzed to compute the dragging force on the released cell (see methods). **F**. A binding kinetic assay was conducted to observe macrophages on KP cells with and without anti-CD11c (1 µg/mL) using an optical tweezer to drive macrophage rolling over the KP cells. The left panel shows a whisker-box plot of quartiles of time between cell-cell contact and adhesion force exceeding 100pN in the indicated condition. The right panels show successive images from contact to adhesion, with the tweezer force direction indicated by an arrow. **G**. The number of aggregates and the total area of GFP+ objects were quantified while coculturing 2500 KP-GFP tumor cells with 5000 AMØ in the presence of increasing concentrations of anti-CD11c or its µcontrol. Images were acquired every 3 hours during the first 130 hours using an IncuCyte. Each

colored curve corresponds to a different concentration of anti-CD11c. The experiment was conducted three times (N=3).

Supplemental movies

Supplementary video 1 to **3.** They correspond to Fig. 1. 5000 KP-GFP cells alone (Supplementary video 1), 5000 KP-GFP + 5000 AMØ (Supplementary video 2), 5000 KP-GFP + 5000 BM-Mo (Supplementary video 3)

Supplementary video 4: 3D stimulation of the surface of the growing spheroid corresponding to Fig. 4E (2500 KP-GFP + 5000 AMØ).

Supplementary video 5 and 6: they correspond to Fig. 5 E. Videos of the rupture force assay of KP cell-macrophage interactions in a laminar flow chamber in the absence (**5**) and the presence (**6**) of anti-CD11c (1 µg/mL), illustrating the examples given in the Fig. 5E. **Supplementary video 7 and 8**: They correspond to Fig. 5F and the Supplementary Fig. 4 and 5 of macrophages rolling on KP cells in the absence (Supplementary video 7) and the presence of anti-CD11c (1 µg/mL) (Supplementary video 8) A single optical tweezer has been used for driving the macrophage rolling over the KP cells.

Supplementary video 9: video of a Z-stack corresponding to supplementary Fig. 1C.

Supplementary Figures

Supplementary Fig. 1. Image acquisition and processing of spheroids of tumors

A. Graph showing the percentage of $Ki67^{+}$ cells among $CD45^{-}$ cells after dissociation of all spheroids present in 12 wells of KP alone or KP with AMØ on days 3 and 7.

B. Images of a 3-day-old KP-GFP spheroid's equatorial section are displayed for each indicated channel. During the last 4 hours, EU was added to the cultures to label RNA synthesis. The spheroids were fixed, stained with Hoechst, and cleared using the Trapoïd device. The clearing procedure enabled accurate imaging of the entire spheroid by confocal microscopy. For example, individual nuclei in the center of the spheroid can be seen through Hoechst staining.

C. The Trapoïd device design is shown from left to right, including the positioning of the spheroid within the arrow of the device. A snapshot of the device with wells filled with blue dye is provided to visualize the connections.

D. Principle of the method used to quantify 3D images. The top row shows an XY median

plane KP-GFP spheroid co-cultured with Tomato AMØ, stained with Hoechst and EdU647, which were acquired after clearing performed in the Trapoïd device (as shown in Fig. 2). The bottom row shows the nuclei seeds detected in the median plane, and the segmented images obtained for each fluorescence channel are displayed.

Supplementary Fig. 2. Aggregation process and structure of the aggregates

A: Description of the aggregation-growth process on a substrate for the cancer cells. The KP cancer cell adhesion properties first become mature. Then, the cells aggregate into a growing aggregate spread on the substrate, which eventually reorganizes into a structured compact spheroid. Green cells correspond to proliferating cells exposed to relatively high concentrations of nutrients. Yellow cells are much less proliferating and are exposed to lower nutrient concentration levels. Red cells are dying cells.

B-D: Particle based simulations for KP cells (in blue) adhering to each other and AMØs (in red) not adhering to each other. KP cells and AMs adhere to each other. Different structures are obtained for different values of the KP-AMØ adhesion. **B.** Adhesion KP-KP stronger than KP-AMØ. **C**. Adhesion KP-KP same as KP-AMØ. **D.** Adhesion KP-KP weaker than KP-AMØ.

E: Concentration profile of the nutrients in an aggregate and its vicinity. The concentration normalized by the concentration far from the aggregate (n/n_∞) is displayed in the function of the distance from the center of the aggregate (*radius*). We consider the nutrient concentration in the KP cells bulk part in green, in the layer of macrophages in red, and outside the aggregate in blue. The critical concentration that controls cell proliferation and death is displayed as a dashed line.

The curves were produced using the same parameters as in the simulation.

Supplementary Fig. 3. Schematic description of the architecture of the physical model and the numerical algorithm

A. Architecture of the physical model. Each aggregate is considered as an object *per se* submitted to forces. The motions of the objects are modeled using a particle-based type model. Each aggregate is also growing. This growth depends on the nutrient profile inside the aggregate, introduced with a continuous formalism. Last, aggregates may fuse after contact, with probabilities that depend on energy barriers.

B: Numerical algorithm. The program is initialized by randomly placing the KP cells and the macrophages in the lower spherical part of the well. Then a global loop computes the position of the cells and of the aggregates at each time step. To do so, a first loop on the aggregates and cells is created that calculates the growth of each aggregate. Then, a second loop on the aggregates and cells considers the forces acting on the aggregates and the

displacement caused by these forces. Eventually, a last loop on the aggregates and cells considers the maturation of the adhesion, the compaction, and the fusions.

Supplementary Fig. 4. **Kinetic of macrophages binding to KP cells using optical tweezers**

A single optical tweezer was used to drive the macrophage rolling over the KP cells in the four examples B-E, supplementing the A shown in Fig. 5F. Successive images, from the initial contact to the adhesion, are shown with the indication of the tweezer force direction, time, and distance from the cell-cell contact event.

Supplementary Fig. 5. **Blocking CD11c alters the kinetic of macrophage binding to KP cells**

A single optical tweezer was used for driving the macrophage rolling over the KP cells in the presence of an anti-CD11c mAb (1 mg/mL) in the two examples A and B supplementing the Fig. 5F.

Supplementary Fig. 6. CD11c+ cells are initially localized in contact to tumor cells before being excluded from the tumor.

Haematoxylin and eosin (H&E) staining of tumor lesions and IHC staining (anti-CD11c)7 days (**A**) or 14 days (**B**) after the injection of KP cells. Arrows indicate CD11c+ cells.

Supplementary Fig. 7. **IHC staining highlighting CD11c+ macrophages in close contact with tumor cells**

NSCLC sections were stained for macrophage marker CD68 (green), CD11c (red), keratin (white), and nuclei (cyan). Scale bar is 100µm.

Supplementary Fig. 8. Graphical abstract

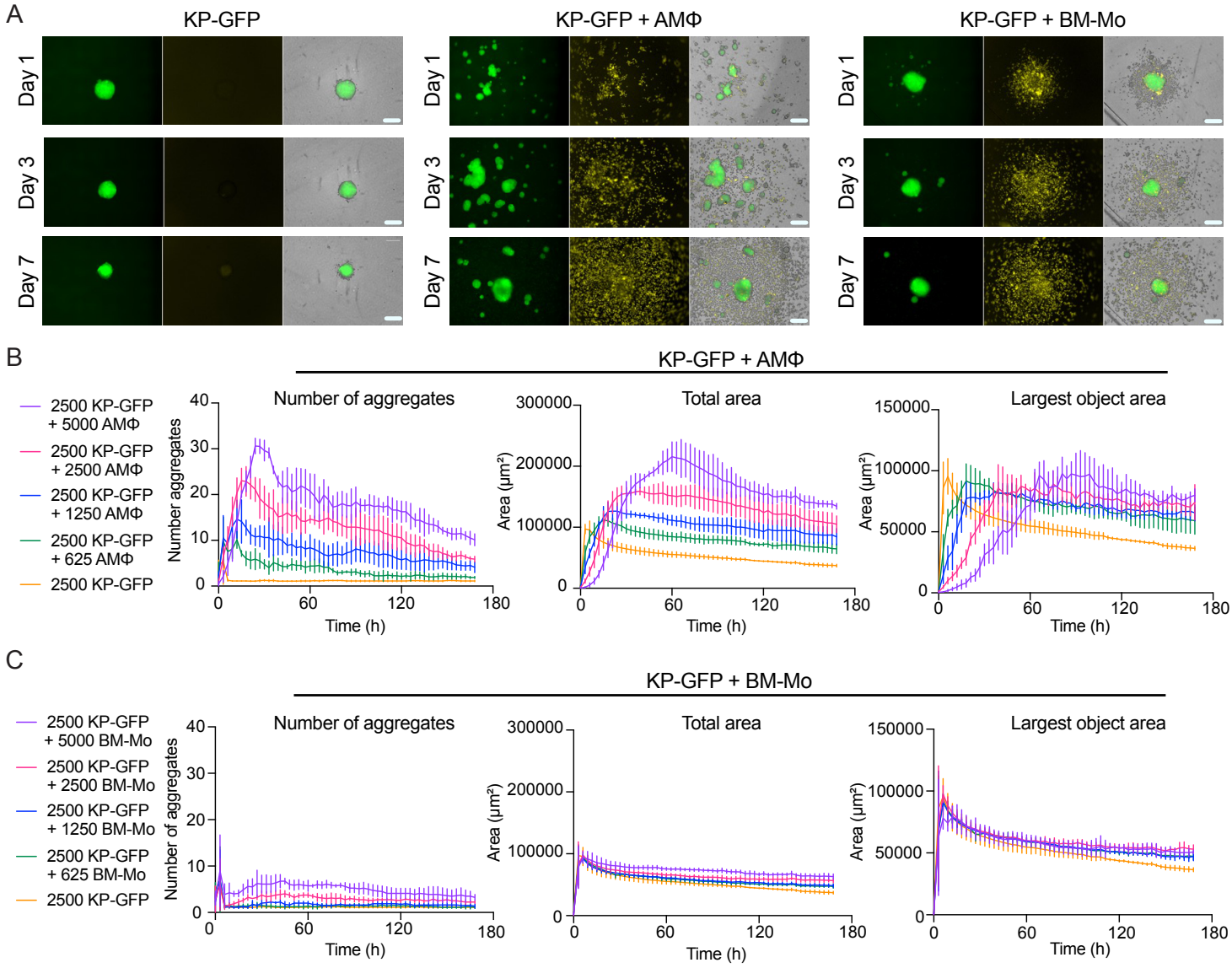

Fig. 1. Evolution of 3D tumor spheroids cultured with alveolar macrophages or monocytes

A. Representative images from movies of 2500 KP-GFP tumor cells co-cultured with 5000 BM-Mo, 5000 AMØ, or alone on days 1, 3, and 7 are shown (extracted from Supplementary video 1 to 3). Myeloid cells were prepared from transgenic mice expressing a membrane-targeted dimer Tomato. The images were acquired over several days with an InCucyte microscope in the GFP and Tomato channels and light transmission. Scale bar = 200µm

B-C. Graphs show the quantifications of the number of aggregates, total area, and largest object area from co-cultures with AMØ or BM-Mo. Images were taken every 3 hours during the first 168 hours of culture. The mean of 3 independent experiments is represented by each colored curve, which corresponds to a different number of AMØ or monocytes.

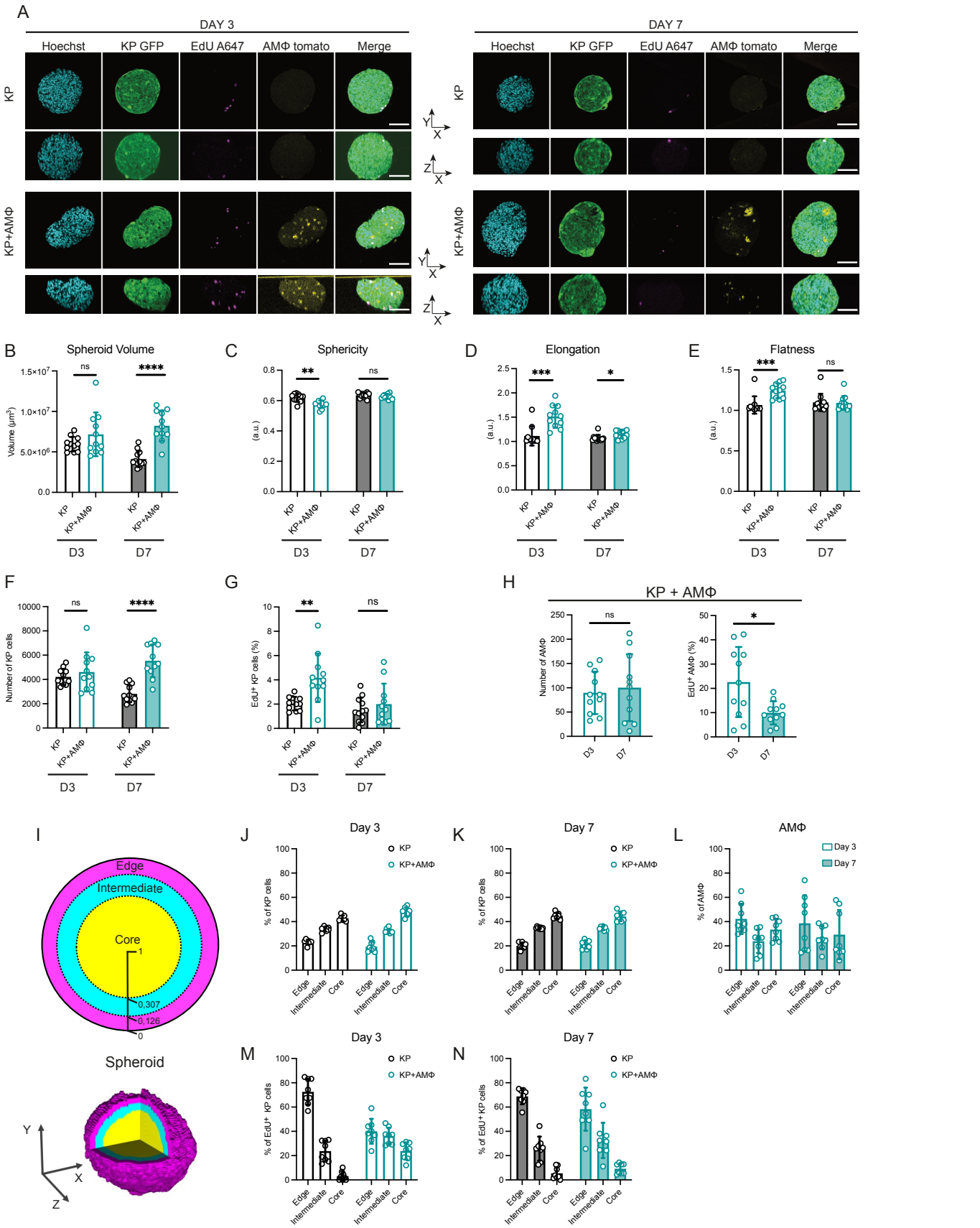

Fig. 2. Spatial quantification of the evolution of tumor spheroid growth in the presence or absence of alveolar macrophages

A. Representative images of KP-GFP spheroids co-cultured with AMØ or alone on days 3 and 7. EdU was added to the cultures for the last four hours to identify the proliferating cells present in the spheroids. The spheroids were fixed, stained with Hoechst, cleared, and analyzed using confocal microscopy. Complete 3D reconstructions were built using stacks of spheroid images acquired every 2 µm. The XY and ZX median planes are presented here. Scale bar = 100µm.

B-H. Quantifications of the 3D spheroid reconstitutions on days 3 and 7 were performed using algorithms developed in Fiji (see Material and Methods) to achieve cell segmentation and measure the indicated parameters. The sphericity was calculated using the formula Sph=36πV2/S3, where V is the volume and S is the surface of the aggregate. The results were obtained from three independent experiments, with 10 to 12 spheroids per condition. Unpaired t-test *P≤0.05, **P≤0.01, ***P≤0.001.

I. Spheroid representation in 2D and 3D. Each spheroid was approximated as a sphere and divided into three concentric regions of equal volume.

J-N. Graphs showing the percentage of (**J**-**K**) KP cells, (**M**-**N**) proliferating KP cells and (**L**) AMØ in each region on days 3 and 7.

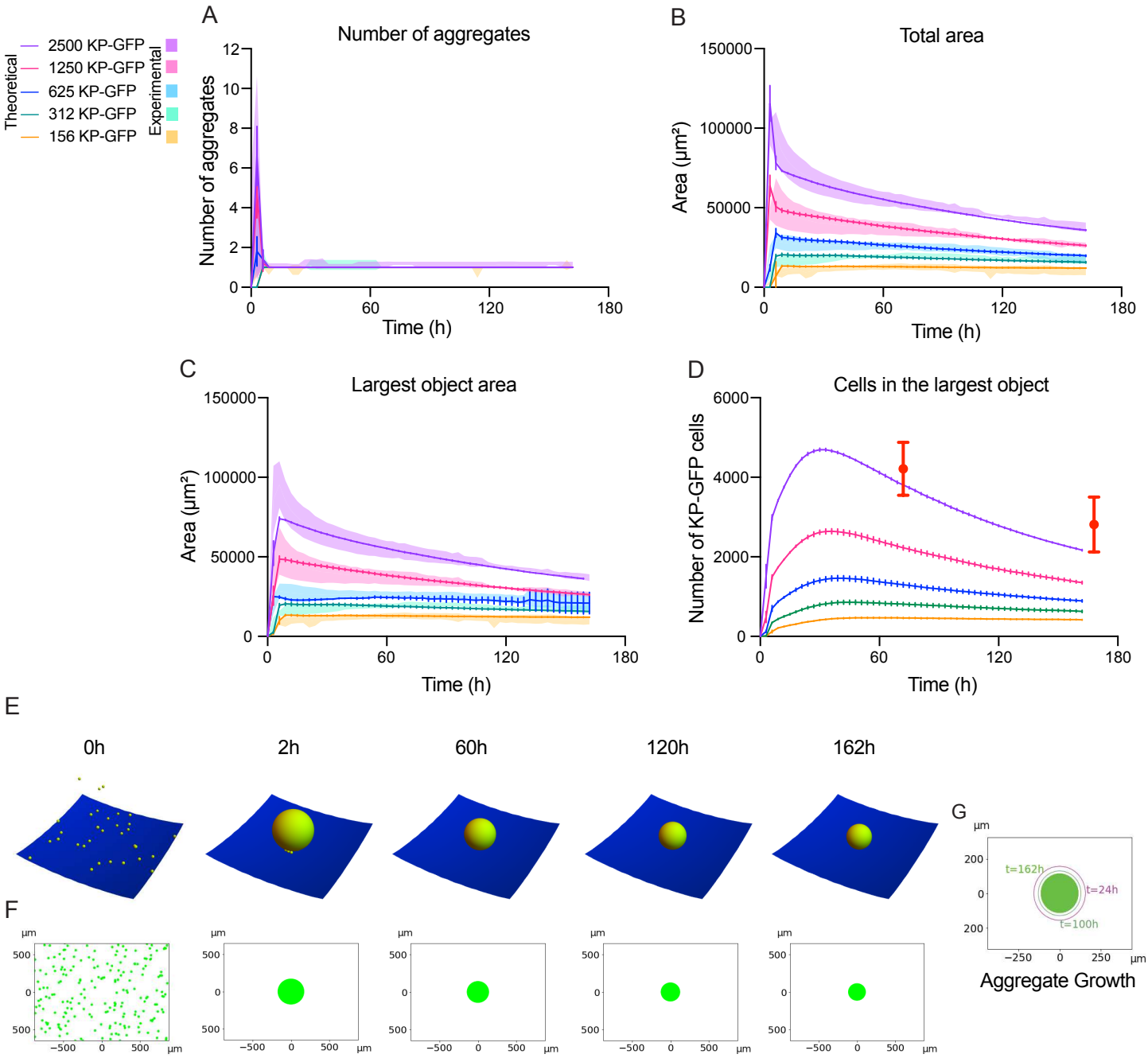

Fig. 3. Comparison between the experimental data and the 3D simulations of the evolution of KP growth in the absence of macrophages

A-D. The graphs display (**A**) the number of aggregates, (**B**) the total area of GFP+ objects, (**C**) the largest object area and (**D**) the number of KP cells in the largest object over time from 0 to 175h co-culture. The two red points with error bars represent the comparison between simulation and experimental results obtained by confocal imaging quantification of cleared spheroids obtained after seeding of 2500 KP-GFP cells collected at 72h (day 3) and 168h (day 7). Experimental curves are presented with shaded surfaces representing standard errors (N=3 independent experiments). Simulations obtained through mathematical modeling are shown as plain lines with vertical bars indicating standard errors. Each colored curve corresponds to a different number of KP cells seeded at t = 0. The same parameters were applied to the mathematical modeling, which generates some variation upon repeats due to the stochasticity introduced. The results obtained by both approaches are overlaid.

E-F. Representation of KP spheroid surface growth by (**E**) a 3D simulation and (**F**) an XY projection at five different timepoints. **G**. Overlay in 2D of the size of the largest object at three timepoints based on the mathematical modeling.

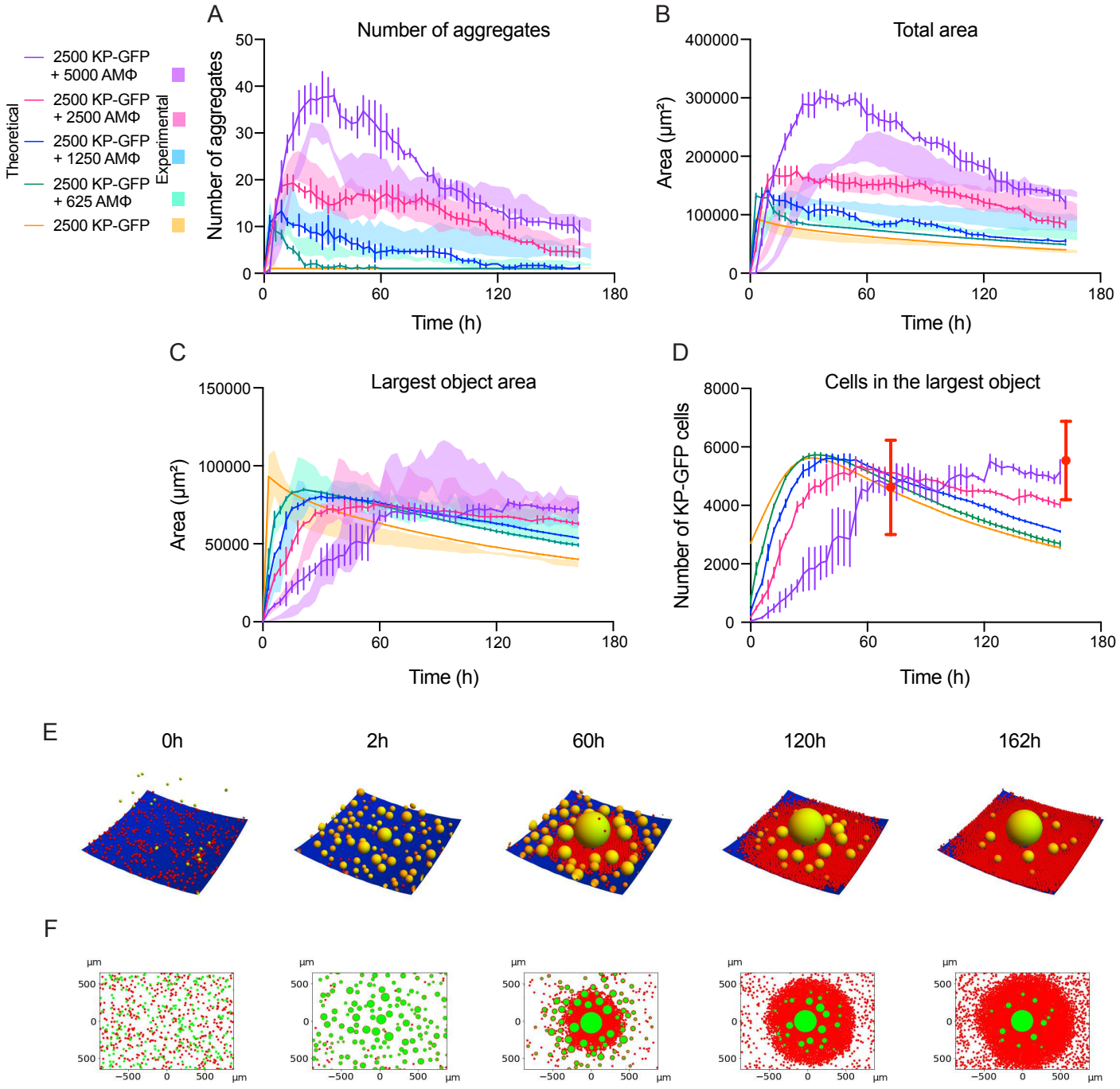

Fig. 4. Comparison between the experimental data and the simulations in 3D of the evolution of KP growth in the presence of increasing numbers of macrophages

A-D. Graphs showing (**A**) the number of aggregates, (**B**) the total area of GFP+ objects, (**C**) the largest object area and (**D**) the number of KP cells in the largest object over time from 0 to 175h co-culture. Two red dots with error bars represent the experimental results obtained by confocal imaging quantification of cleared spheroids obtained after seeding 2500 KP-GFP cells with 5000 macrophages harvested at 72h (day 3) and 168h (day 7). The experimental curves display shaded areas to represent the standard deviation, while simulations obtained through mathematical modeling are shown as plain lines with vertical bars to indicate the standard error. The experiments involved seeding 2500 KP-GFP tumor cells per well with varying numbers of freshly isolated alveolar macrophages (0, 625, 1250, 2500, and 5000 AMØ). Each colored curve corresponds to a different number of alveolar macrophages initially seeded. During the first 175 hours of culture, images were captured using an IncuCyte and the same parameters were used for mathematical modeling. The results obtained from both approaches are overlaid. **E-F**. The growth of the KP-GFP cells and AMØ spheroid surface is represented in 3D simulation (E) and XY plane projection (F) at five different timepoints.

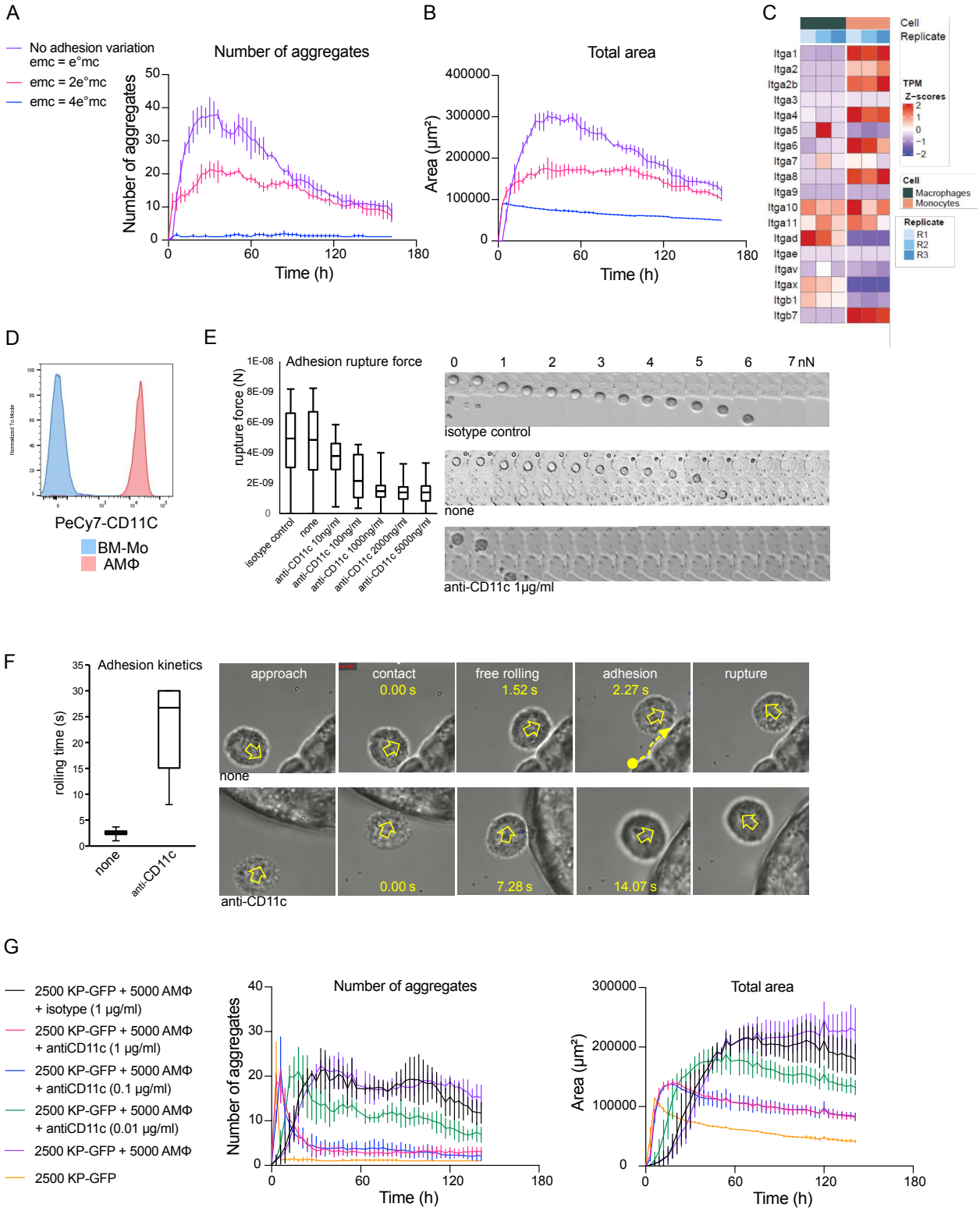

Fig. 5. Blocking CD11c inhibits the positive impact of alveolar macrophages on tumor growth in vitro.

A-B. Simulations of the evolution of (**A**) the number of aggregates and (**B**) the total area of GFP+ objects when reducing the interaction forces between macrophages and tumor cells.

C. Heat map analysis of RNAseq data obtained from freshly isolated bone marrow monocytes and alveolar macrophages. Here is displayed the TPM for members of the integrin family. N = 3 replicates. The gene *Itgax* encodes for the CD11c protein. **D**. Flow cytometry histogram of the CD11c surface expression in bone marrow monocytes and alveolar macrophages. **E**. Rupture force assay of KP cell-macrophage interactions in a laminar flow chamber in the presence of anti-CD11c at varying concentrations. The left panel shows a whisker-box plot of quartiles of dragging force values at the cell-cell interaction rupture event under the indicated conditions. The right panels show successive images displayed as tiles under the indicated conditions, with the dragging force scale detailed at the top. AMØ were gently loaded onto KP cells seeded in adhesive flow chambers in the presence of the indicated antibodies at various concentrations for 10 minutes and submitted to an increasing flow rate synchronized with image acquisition. The image series were analyzed to compute the dragging force on the released cell (see methods). **F**. A binding kinetic assay was conducted to observe macrophages on KP cells with and without anti-CD11c (1 µg/mL) using an optical tweezer to drive macrophage rolling over the KP cells. The left panel shows a whisker-box plot of quartiles of time between cell-cell contact and adhesion force exceeding 100pN in the indicated condition. The right panels show successive images from contact to adhesion, with the tweezer force direction indicated by an arrow. **G**. The number of aggregates and the total area of GFP+ objects were quantified while coculturing 2500 KP-GFP tumor cells with 5000 AMØ in the presence of increasing concentrations of anti-CD11c or its µcontrol. Images were acquired every 3 hours during the first 130 hours using an IncuCyte. Each colored curve corresponds to a different concentration of anti-CD11c. The experiment was conducted three times (N=3).

Supplementary Figures

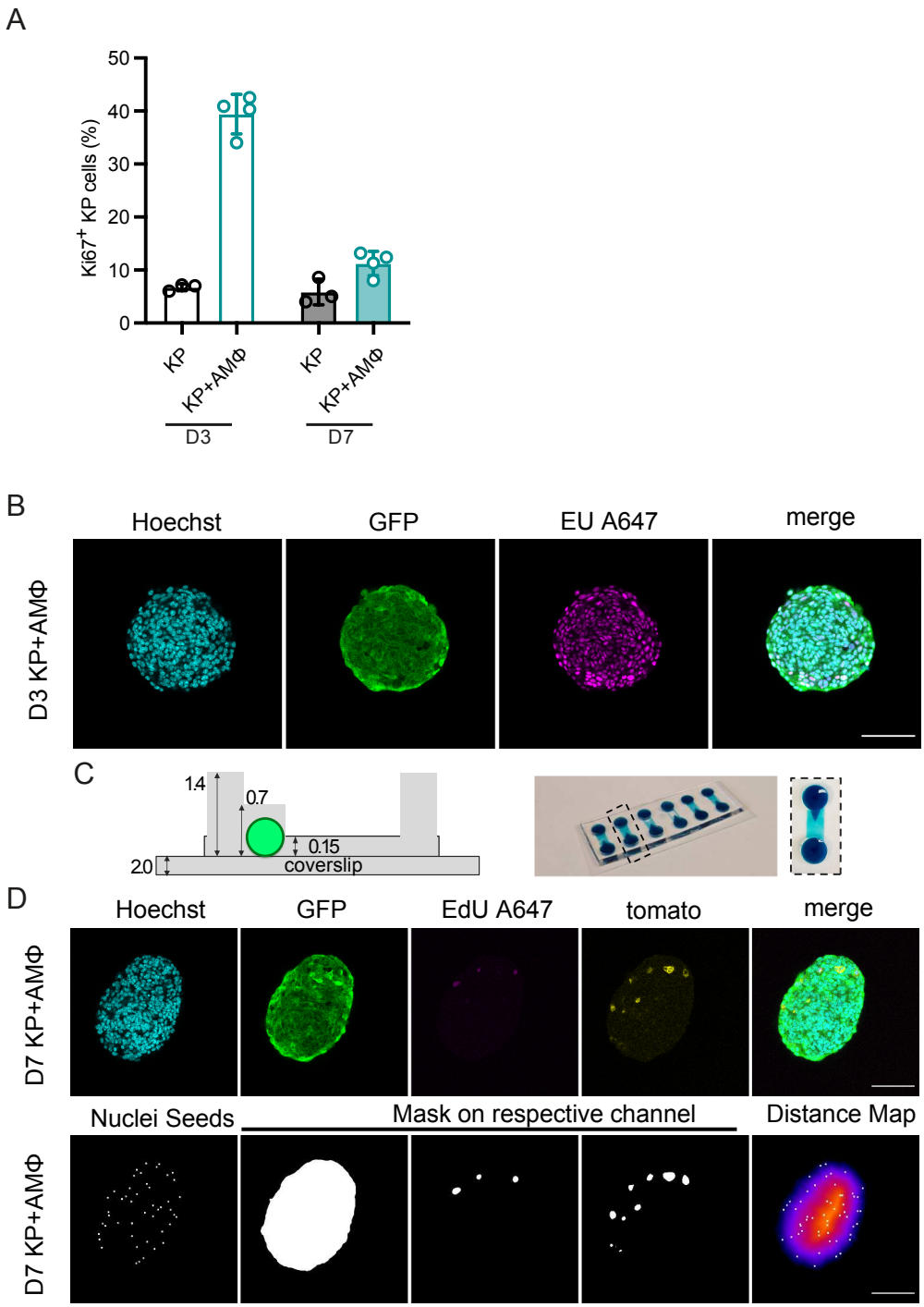

Supplementary Fig. 1. Image acquisition and processing of spheroids of tumors

A. Graph showing the percentage of Ki67$^+$ cells among CD45$^-$ cells after dissociation of all spheroids present in 12 wells of KP alone or KP with AMØ on days 3 and 7.

B. Images of a 3-day-old KP-GFP spheroid's equatorial section are displayed for each indicated channel. During the last 4 hours, EU was added to the cultures to label RNA synthesis. The spheroids were fixed, stained with Hoechst, and cleared using the Trapoïd device. The clearing procedure enabled accurate imaging of the entire spheroid by confocal microscopy. For example, individual nuclei in the center of the spheroid can be seen through Hoechst staining.

C. The Trapoïd device design is shown from left to right, including the positioning of the spheroid within the arrow of the device. A snapshot of the device with wells filled with blue dye is provided to visualize the connections.

D. Principle of the method used to quantify 3D images. The top row shows an XY median plane KP-GFP spheroid co-cultured with Tomato AMØ, stained with Hoechst and EdU647, which were acquired after clearing performed in the Trapoïd device (as shown in Fig. 2). The bottom row shows the nuclei seeds detected in the median plane, and the segmented images obtained for each fluorescence channel are displayed.

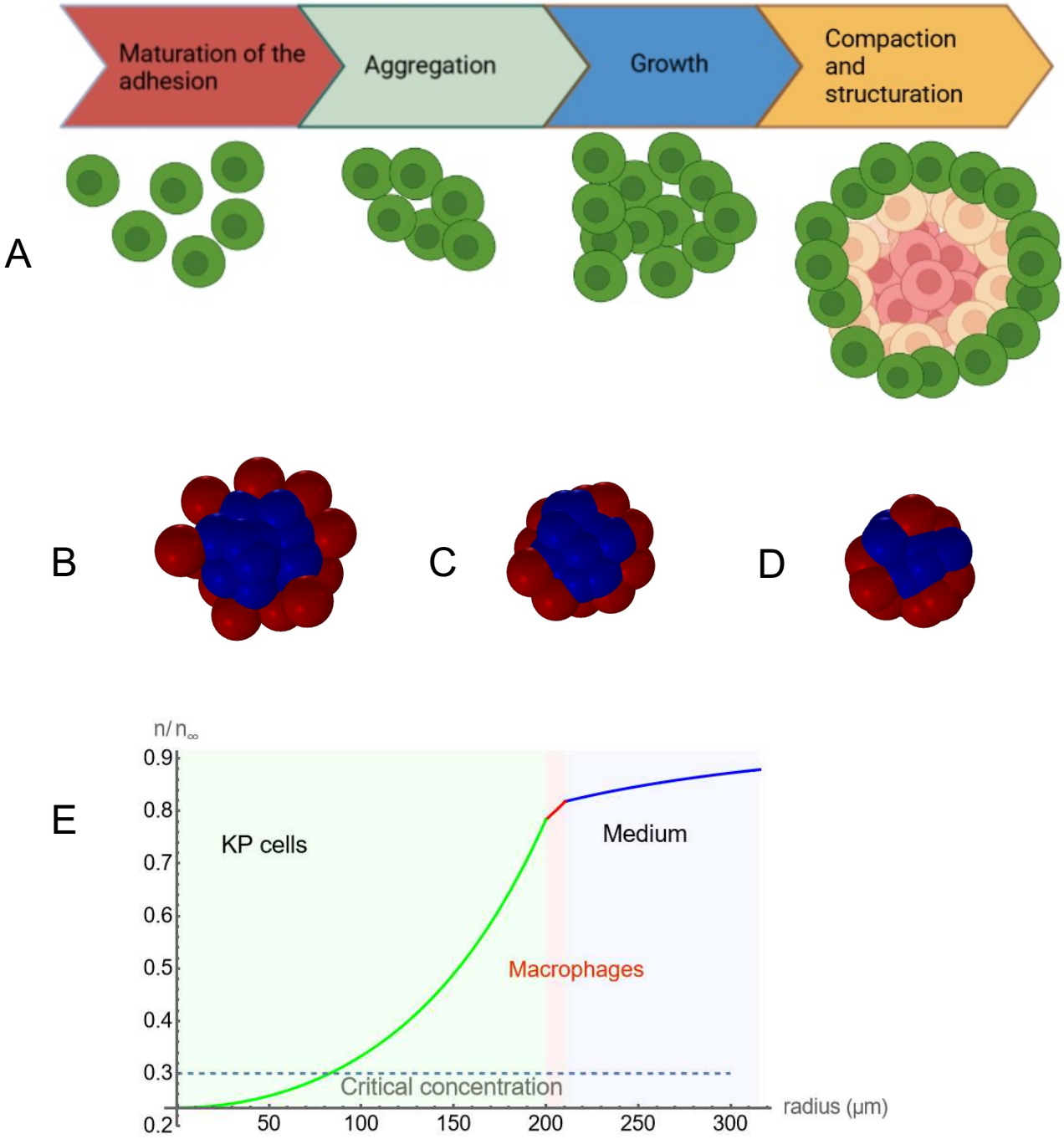

Supplementary Fig. 2. Aggregation process and structure of the aggregates

A: Description of the aggregation-growth process on a substrate for the cancer cells. The KP cancer cell adhesion properties first become mature. Then, the cells aggregate into a growing aggregate spread on the substrate, which eventually reorganizes into a structured compact spheroid. Green cells correspond to proliferating cells exposed to relatively high concentrations of nutrients. Yellow cells are much less proliferating and are exposed to lower nutrient concentration levels. Red cells are dying cells.

B-D: Particle based simulations for KP cells (in blue) adhering to each other and AMØs (in red) not adhering to each other. KP cells and AMs adhere to each other. Different structures are obtained for different values of the KP-AMØ adhesion. **B.** Adhesion KP-KP stronger than KP-AMØ. **C**. Adhesion KP-KP same as KP-AMØ. **D.** Adhesion KP-KP weaker than KP-AMØ.

E: Concentration profile of the nutrients in an aggregate and its vicinity. The concentration normalized by the concentration far from the aggregate (n/n_∞) is displayed in the function of the distance from the center of the aggregate (*radius*). We consider the nutrient concentration in the KP cells bulk part in green, in the layer of macrophages in red, and outside the aggregate in blue. The critical concentration that controls cell proliferation and death is displayed as a dashed line.

The curves were produced using the same parameters as in the simulation.

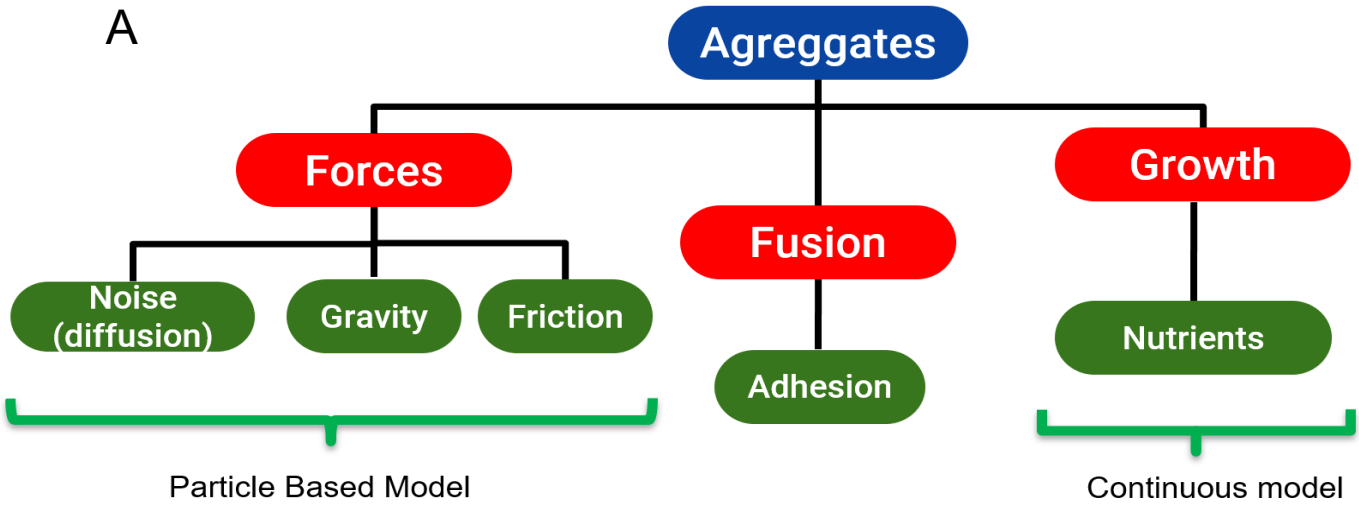

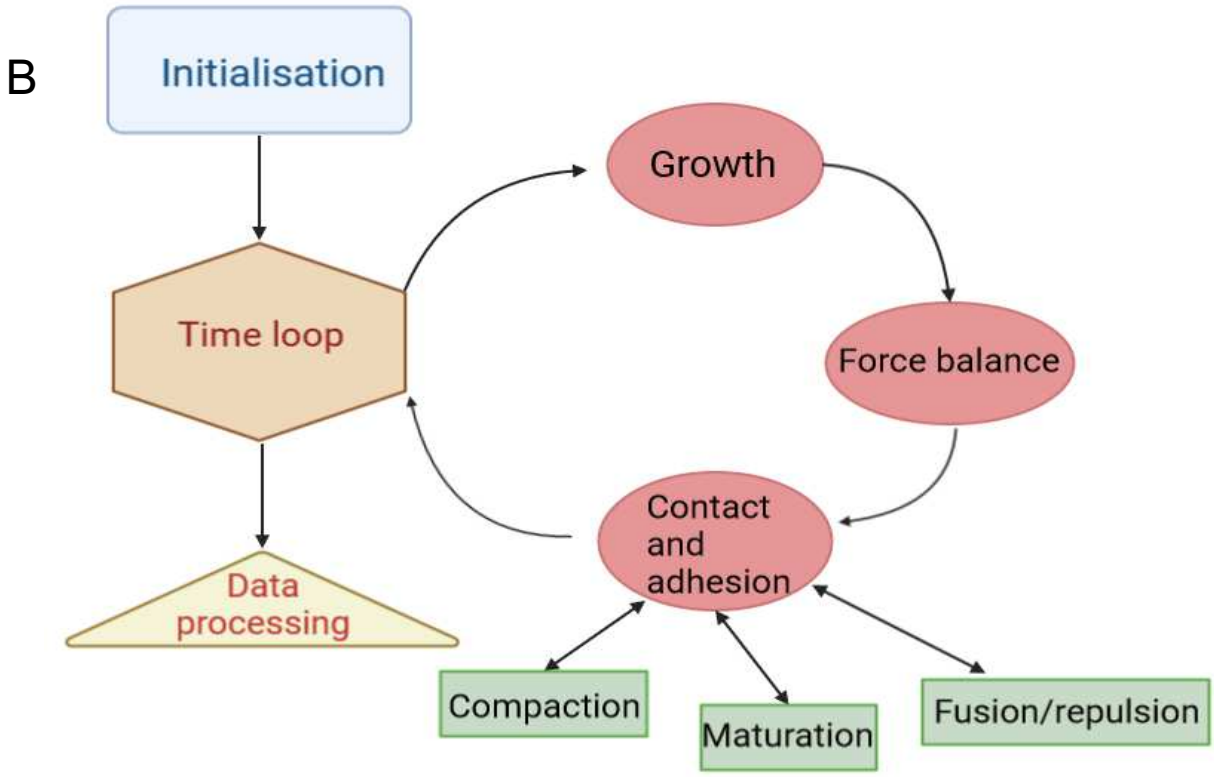

Supplementary Fig. 3. Schematic description of the architecture of the physical model and the numerical algorithm

A. Architecture of the physical model. Each aggregate is considered as an object *per se* submitted to forces. The motions of the objects are modeled using a particle-based type model. Each aggregate is also growing. This growth depends on the nutrient profile inside the aggregate, introduced with a continuous formalism. Last, aggregates may fuse after contact, with probabilities that depend on energy barriers.

B: Numerical algorithm. The program is initialized by randomly placing the KP cells and the macrophages in the lower spherical part of the well. Then a global loop computes the position of the cells and of the aggregates at each time step. To do so, a first loop on the aggregates and cells is created that calculates the growth of each aggregate. Then, a second loop on the aggregates and cells considers the forces acting on the aggregates and the displacement caused by these forces. Eventually, a last loop on the aggregates and cells considers the maturation of the adhesion, the compaction, and the fusions.

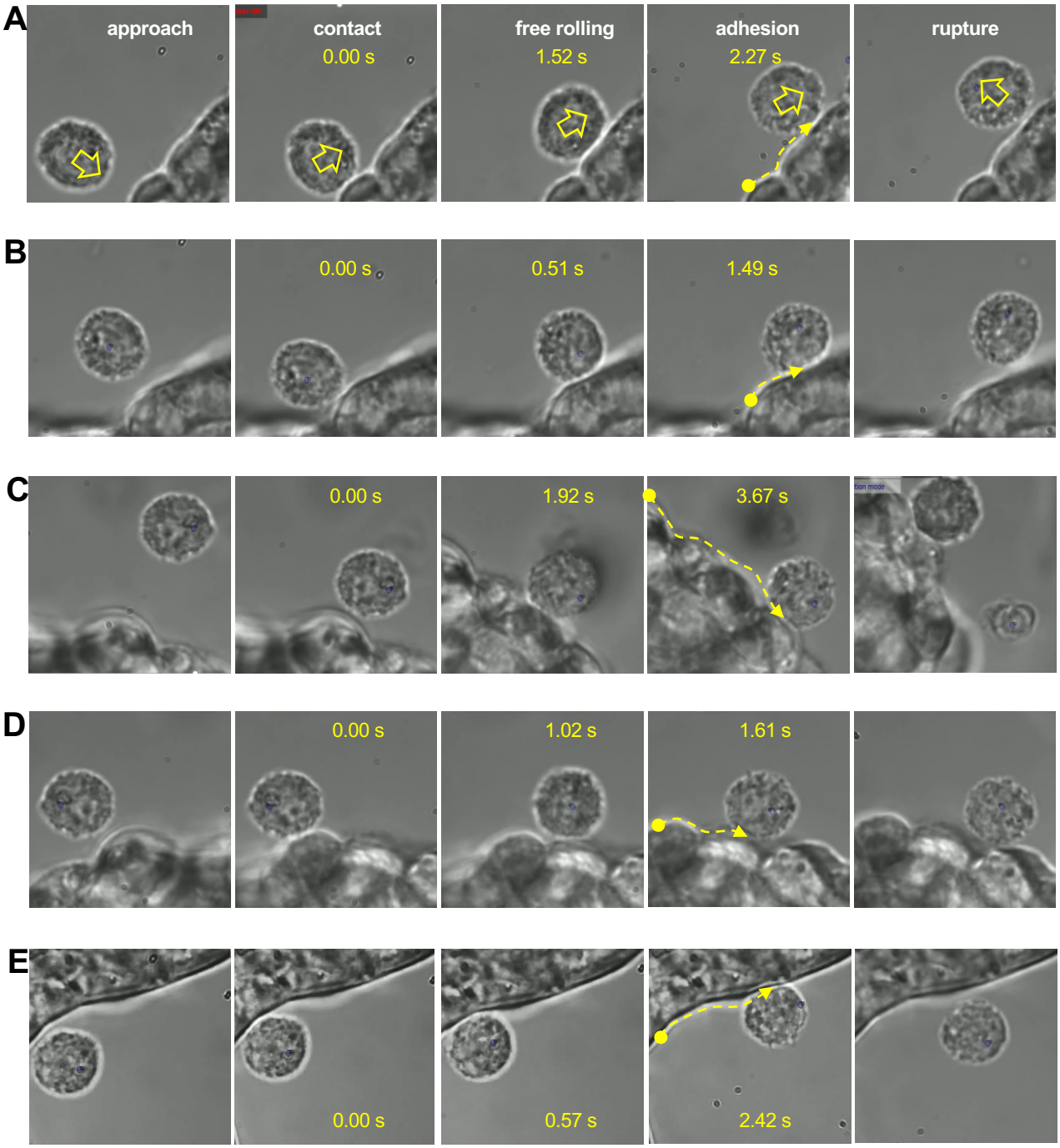

Supplementary Fig. 4. **Kinetic of macrophages binding to KP cells using optical tweezers**

A single optical tweezer was used to drive the macrophage rolling over the KP cells in the four examples B-E, supplementing the A shown in Fig. 5F. Successive images, from the initial contact to the adhesion, are shown with the indication of the tweezer force direction, time, and distance from the cell-cell contact event.

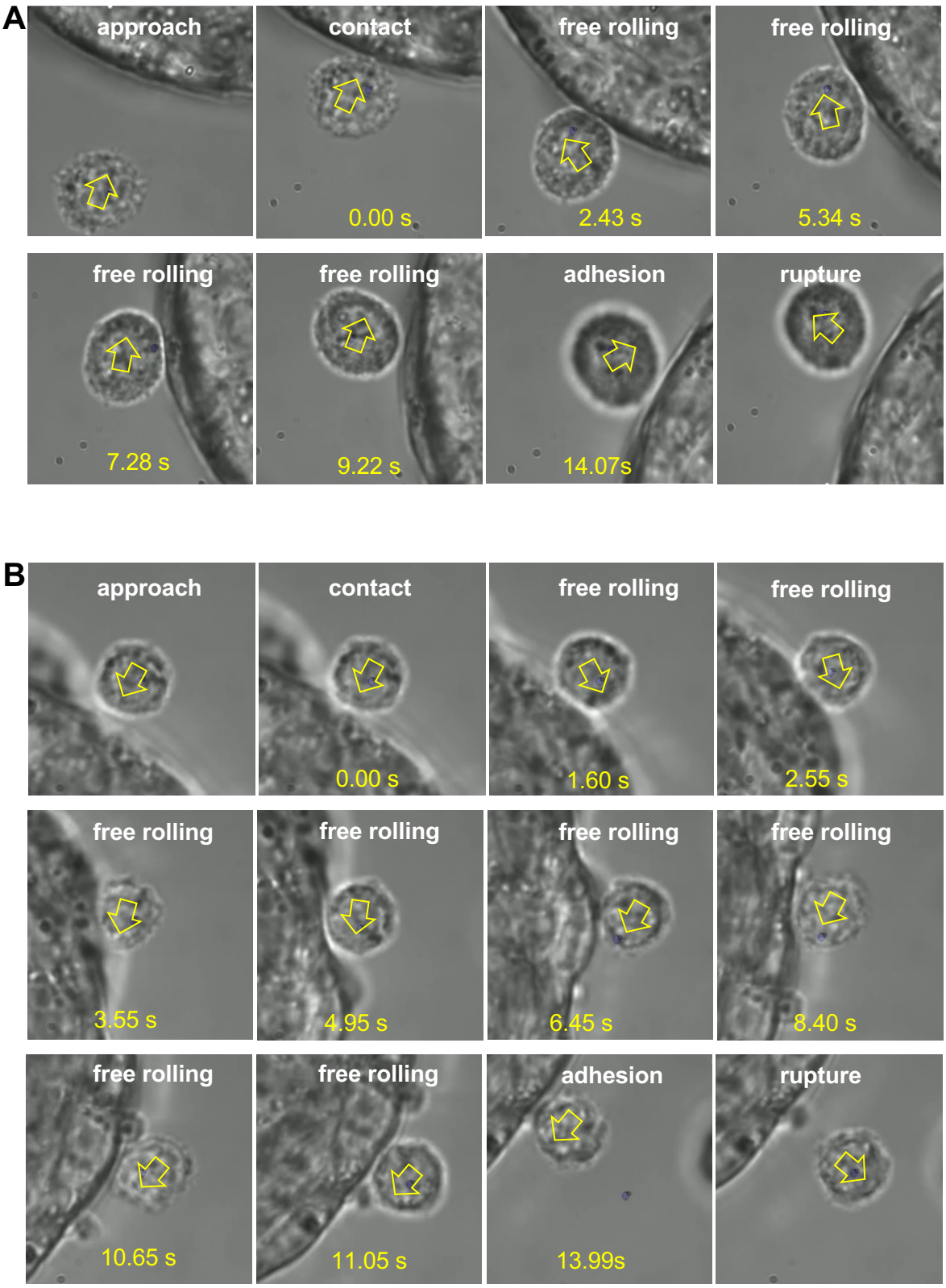

Supplementary Fig. 5. Blocking CD11c alters the kinetic of macrophage binding to KP cells

A single optical tweezer was used for driving the macrophage rolling over the KP cells in the presence of an anti-CD11c mAb (1 mg/mL) in the two examples A and B supplementing the Fig. 5F.

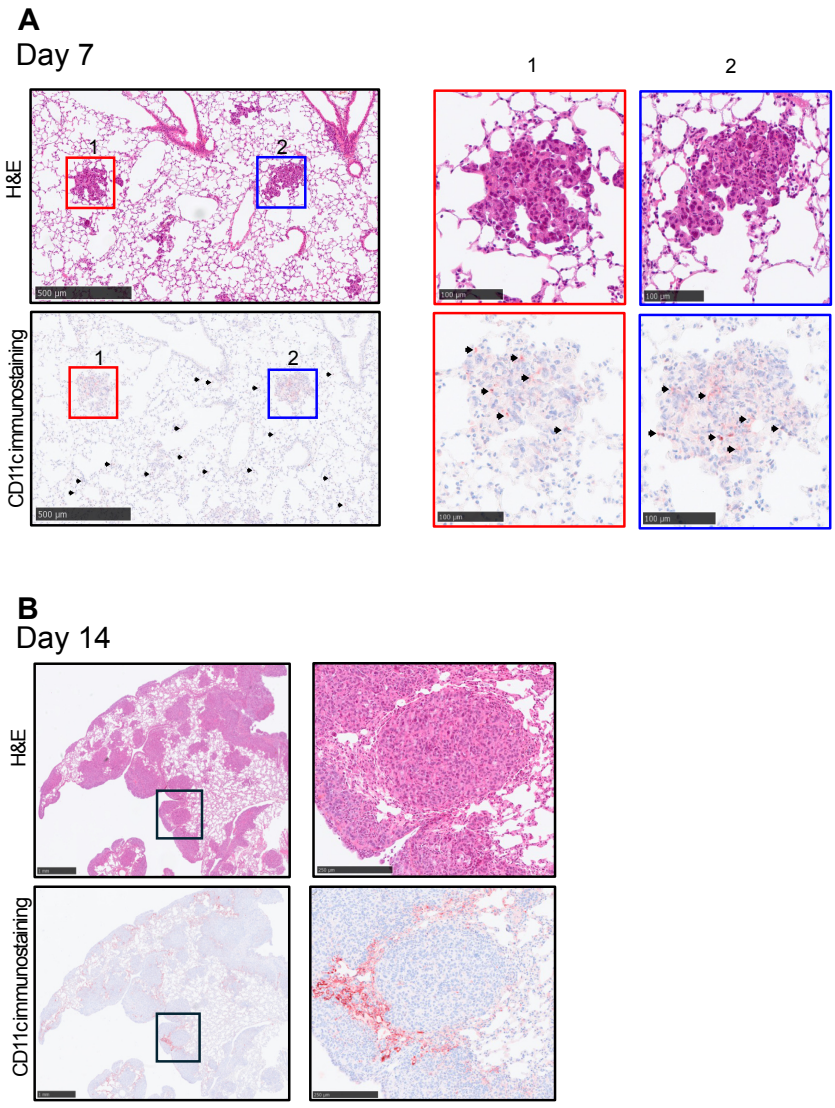

Supplementary Fig. 6. CD11c+ cells are initially localized in contact to tumor cells before being excluded from the tumor.

Haematoxylin and eosin (H&E) staining of tumor lesions and IHC staining (anti-CD11c)7 days (**A**) or 14 days (**B**) after the injection of KP cells. Arrows indicate CD11c+ cells.

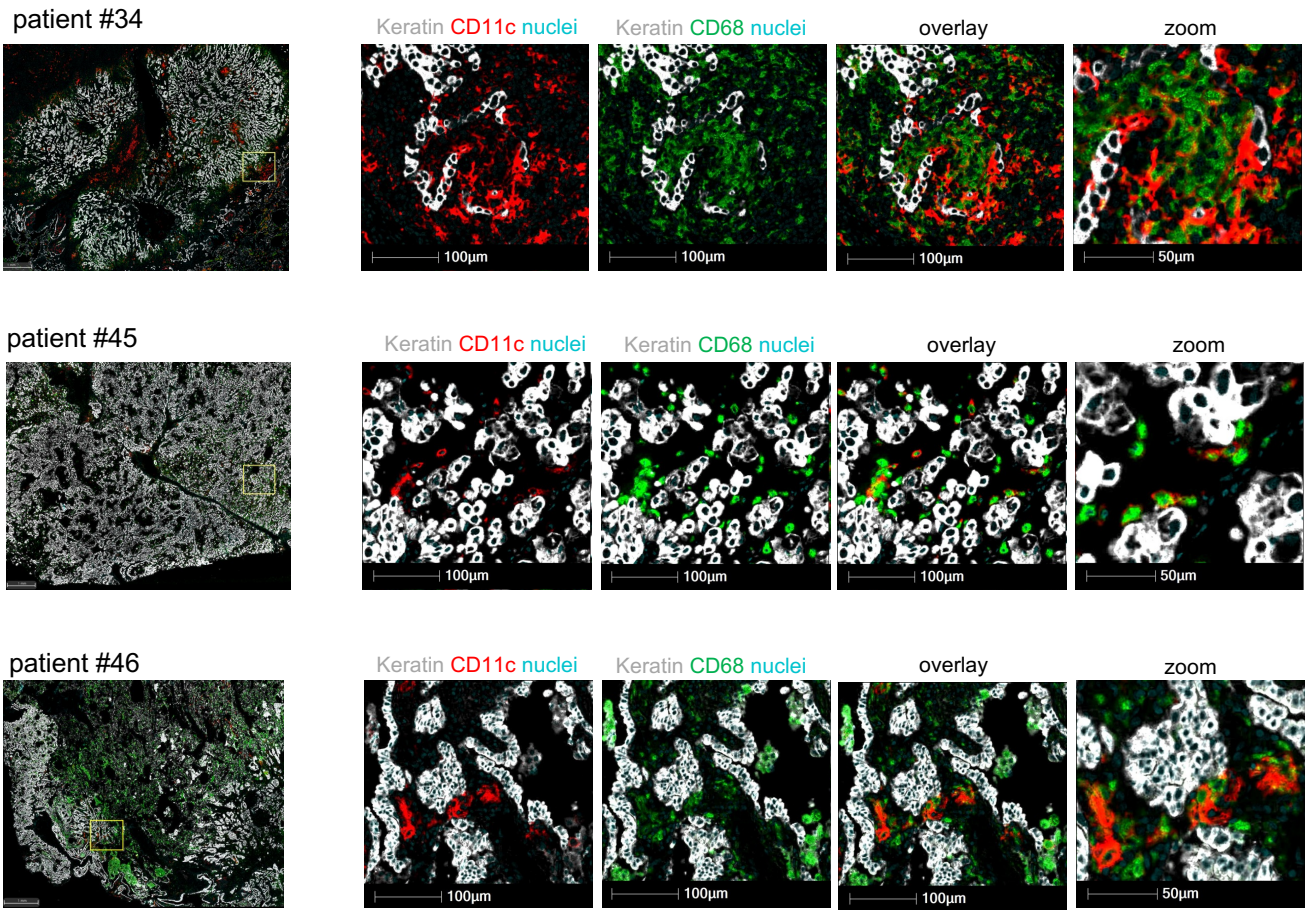

Supplementary Fig. 7. IHC staining highlighting CD11c+ macrophages in close contact with tumor cells

NSCLC sections were stained for macrophage marker CD68 (green), CD11c (red), keratin (white), and nuclei (cyan). Scale bar is 100µm

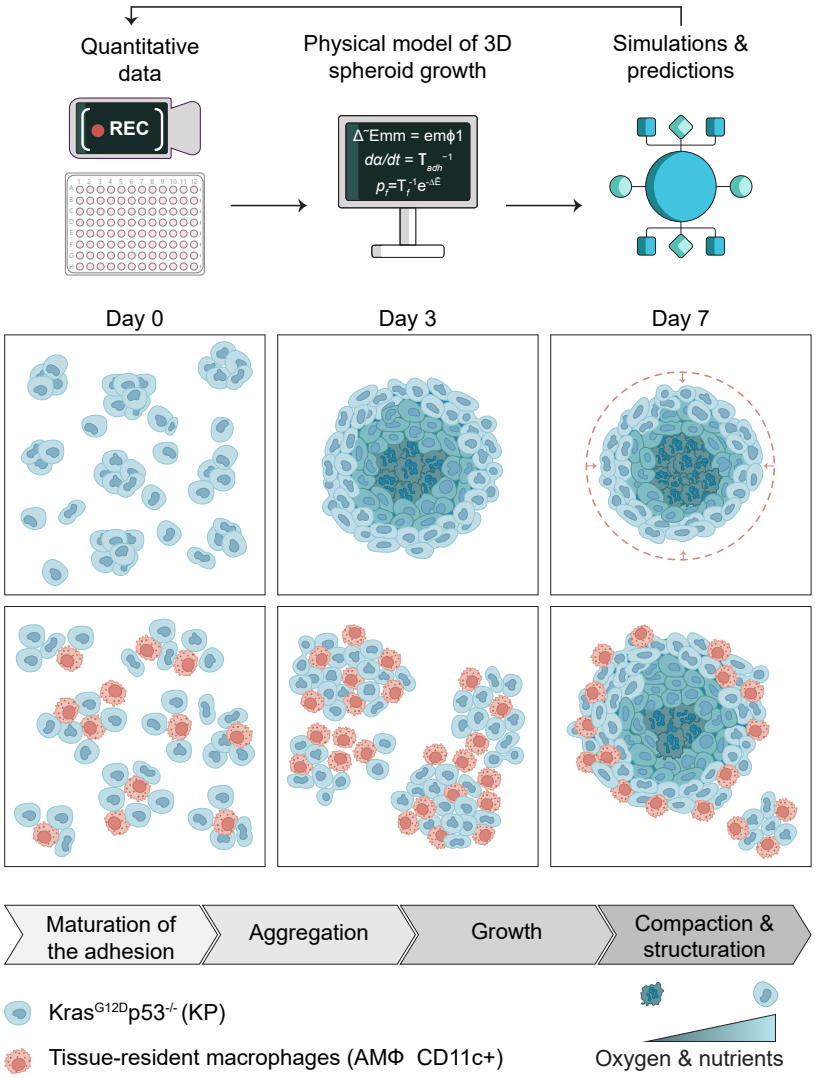

Supplementary Fig. 8.Graphical Abstract

Supplementary Files

This is a list of supplementary files associated with this preprint. Click to download.

- SupplementarymaterialsNikolicetal.pdf
- suppvideo1KP.mp4
- suppvideo2KPmacro.mp4
- suppvideo3KPmono.mp4
- suppvideo4simulation.mov
- Suppvideo5.mov
- Suppvideo6.mov
- Suppvideo7.avi
- Suppvideo8.avi
- suppvideo9macroZstack.avi